

Fermi National Accelerator Laboratory

FERMILAB-FN-595

Design and Study of Accelerator Lattices without Transition

S.Y. Lee, K.Y. Ng and D. Trbojevic

*Fermi National Accelerator Laboratory
P.O. Box 500, Batavia, Illinois 60510*

October 1992

Submitted to *Physical Review A*

Disclaimer

This report was prepared as an account of work sponsored by an agency of the United States Government. Neither the United States Government nor any agency thereof, nor any of their employees, makes any warranty, express or implied, or assumes any legal liability or responsibility for the accuracy, completeness, or usefulness of any information, apparatus, product, or process disclosed, or represents that its use would not infringe privately owned rights. Reference herein to any specific commercial product, process, or service by trade name, trademark, manufacturer, or otherwise, does not necessarily constitute or imply its endorsement, recommendation, or favoring by the United States Government or any agency thereof. The views and opinions of authors expressed herein do not necessarily state or reflect those of the United States Government or any agency thereof.

Design and Study of Accelerator Lattices without Transition

S.Y. Lee,* K.Y. Ng, and D. Trbojevic†

Fermi National Accelerator Laboratory,‡ P.O. Box 500, Batavia, IL 60510

(Received October 1992)

(Submitted to Physical Review A)

*Permanent address: Department of Physics, Indiana University, Bloomington, IN 47405.

†Present address: Brookhaven National Laboratory, Upton, Long Island, NY 11973.

‡Operated by the Universities Research Association, Inc., under contract with the U. S. Department of Energy.

ABSTRACT

Medium energy accelerators are often confronted with problems during transition energy crossing, such as longitudinal microwave instability and nonlinear synchrotron motion. These problems can be avoided by an accelerator having a negative momentum compaction factor. A modular method for designing a lattice with adjustable momentum compaction factor is presented. The phase advance of the basic flexible momentum compaction module can be adjusted to be an odd multiple of quarter betatron waves. We found that a lattice composed of such modules possesses excellent chromatic properties with smaller dispersions, smaller systematic stopband widths, and smaller sextupole distortion functions. The latest lattice without transition energy crossing for the Fermilab Main Injector is used for a comprehensive lattice study.

I. INTRODUCTION

The deviation of the revolution period ΔT for an off-momentum particle at momentum $p_0 + \Delta p$ relative to that of the synchronous (on-momentum) particle at momentum p_0 and revolution period T_0 is given by

$$\frac{\Delta T}{T_0} = \left(\alpha - \frac{1}{\gamma^2} \right) \frac{\Delta p}{p_0}, \quad (1.1)$$

where the factor $\eta = \alpha - \frac{1}{\gamma^2}$ is called the phase slip factor and γ is the Lorentz relativistic factor for the off-momentum particle. In the above, α is the momentum compaction factor, which measures the path length difference between the off-momentum particle and the on-momentum particle. When the beam particle is accelerated, the phase slip factor changes sign as γ reaches $\gamma_t = \frac{1}{\sqrt{\alpha}}$. This is the moment the particle crosses *transition*.

There are many unfavorable effects on the particle motion around transition energy. The momentum spread of a bunch around transition could become so large that it exceeds the available momentum aperture and beam loss could occur. There is little or no Landau damping against microwave instability near transition [2]. As a result, the bunch area grows due to the space-charge force of the beam as well as due to the wake forces created by the bunch inside the vacuum chamber. Particles with different momenta usually cross transition at different times leading to longitudinal phase space distortions and beam loss. However, if the momentum compaction factor is a negative number, there will not be any transition energy crossing and all the above unfavorable effects will be avoided.

To the lowest order in $\Delta p/p_0$, the momentum compaction factor is related to the horizontal momentum dispersion function D by

$$\alpha = \frac{1}{C_0} \oint \frac{D(s)}{\rho(s)} ds, \quad (1.2)$$

where ρ is the radius of curvature and s is measured along the reference closed orbit which has a total length C_0 . If only a *matched* module of the ring is considered, C_0 will be the length of the module. If each dipole at position i is approximated as a thin element having an average dispersion \bar{D}_i and bending angle θ_i , the momentum compaction factor can be written as

$$\alpha = \frac{1}{\gamma_t^2} \approx \frac{1}{C_0} \sum_{i=\text{dipole}} \bar{D}_i \theta_i. \quad (1.3)$$

The transition gamma will be an imaginary number if the momentum compaction factor α is less than zero. Thus the condition for an imaginary γ_t lattice is to have negative horizontal dispersion through most of the dipoles: $\sum_i \bar{D}_i \theta_i|_{\text{dipole}} < 0$; i.e. $D < 0$ in most of the dipoles.

There are many approaches for the design of an imaginary γ_t or high γ_t lattice, where transition energy crossing during acceleration can be avoided [3–8]. The *harmonic approach* and the *high-tune approach* [3–8] create a systematic stopband to induce dispersion-wave oscillations resulting in a high γ_t . Such a method will give rise to a less controllable dispersion function and the dynamical aperture will therefore be smaller accordingly. On the other hand, the *modular approach* [6–8], introduced by Trbojevic et al [6], uses carefully matched negative dispersion function inside dipoles in each module of the accelerator in order to achieve a negative momentum compaction factor, or an imaginary γ_t .

This report will present a detailed design strategy and a study of the beam dynamics of the imaginary γ_t lattice. The method consists of constructing a module made of two parts: (1) the FODO- (or DOFO-) cell part where the negative dispersion function propagates through the dipoles and (2) the *near- π* matching module [6–8] which connects the FODO (or DOFO) cells with a horizontal betatron phase advance ϕ close to π . The negative values of the horizontal dispersion function in the dipole region determine the value of γ_t . Many advantages of our design, such as the control of the dispersion function, tunable γ_t value, dispersion-free straight sections, small systematic stopband widths, and small sextupole distortion functions will be demonstrated.

The report is organized in the following way. The design method [6] is reviewed in Sec. II, where examples of lattices with different values of the γ_t are presented. In Sec. III, a complete design of an imaginary γ_t lattice for the Fermilab Main Injector is discussed. The compactness of the recent lattice is significantly improved compared to the two designs previously presented [6, 7], due to both the smaller number and smaller sizes of the quadrupole magnets. This lattice provides excellent beam dynamic properties, which are analyzed in Sec. IV. We also discuss the chromaticity-correction scheme, the dependence on momentum, the tunability of the lattice, the betatron-function and the tune dependences on the gradient errors in the main quadrupoles, as well as the quadrupole misalignment sensitivity factors. An analysis of the distortion functions introduced by the chromaticity sextupoles is given in detail because of their vital influence on the dynamical aperture. Our special precautions taken in the lattice

design and in the positioning of the sextupoles lead to small tunes shift dependences on amplitude. As a result, no additional families of harmonic sextupoles are necessary. Tracking results show that the 35,000-turn survival dynamical aperture turns out to be much larger than the 40π mm-mr design requirement. Analytic analysis of the design strategy is given in the appendix.

II. REVIEW OF THE DESIGN METHOD

A. Normalized Dispersion Function

The dispersion function D satisfies a second-order inhomogeneous differential equation of motion,

$$D'' + K_x(s)D = \frac{1}{\rho(s)}, \quad (2.1)$$

where s is the distance measured along the reference orbit with local radius of curvature $\rho(s)$, while

$$K_x = \frac{1}{\rho^2} - \frac{1}{B\rho} \frac{\partial B_y}{\partial x}, \quad (2.2)$$

is the sum of the centrifugal focussing and the quadrupole focussing. Let us define the normalized coordinate system,

$$\chi = \frac{1}{\sqrt{\beta_x}} D = \sqrt{2J} \sin \phi, \quad \xi = \sqrt{\beta_x} D' - \frac{\beta'_x}{2\sqrt{\beta_x}} D = \sqrt{2J} \cos \phi, \quad (2.3)$$

where J is called the dispersion action and ϕ is identical to the horizontal Floquet betatron phase advance in the region where there is no dipole, D and D' are the dispersion function and the derivative of the dispersion function with respect to s , respectively, while β_x and β'_x are respectively the horizontal betatron amplitude function and its derivative [1]. In the thin-element approximation, the function due to a pure bending dipole is therefore given by $\Delta\xi \approx \sqrt{\beta_x}\theta$ and $\Delta\chi = 0$, with a contribution of $\sqrt{\beta_x}\chi\theta/C_0$ to the momentum compaction factor. Outside the dipole ($\rho = \infty$), the dispersion function satisfies the homogeneous equation, so that J is an invariant, with χ and ξ satisfying $\chi^2 + \xi^2 = 2J$, which is a circle. The ξ - χ plot therefore advances by the phase angle ϕ .

B. Design of the Basic Module

To build a module with a negative momentum compaction factor, most of the dipoles should be within the third and fourth quadrants of the ξ - χ normalized dispersion space, where the horizontal dispersion (or the normalized dispersion $\chi = D/\sqrt{\beta_x}$) has negative values. We demand a full symmetry of all Twiss functions within the module with respect to the vertical χ axis. This condition is not a necessary constraint. However, this symmetry does help to control the maximum and minimum of the dispersion function. At the same time, accurate matching of the betatron

functions can be made much easier with fewer number of variables. The first part of the module is made of a FODO (or DOFO) cell or cells with a starting point A , as presented in Fig. 1, which is located on the χ axis of the ξ - χ space. In the appendix, a general analytic analysis of the basic module is given.

1. Maxima of the Positive and Negative Dispersion

To achieve an imaginary γ_t , point A in Fig. 1, located at the center of two consecutive FODO cells, should have a negative value on the χ axis. FODO cells are adjoined with respect to point A with a reflective symmetry. The normalized dispersion function of these FODO (or DOFO) cells fills up symmetrically the third and fourth quadrants of the ξ - χ space up to point B close to the positive ξ axis and point D close to the negative ξ axis. If there are no dipoles in the matching section, points B and D are joined by an arc with the center at the origin. This arc occupies most or all of the first and second quadrants of the ξ - χ space, and it is almost a semicircle with 180° horizontal betatron phase advance. This *near- π* insertion cuts the positive χ axis at the highest value χ_{\max} denoted by point C , which is the reflective symmetric point of the matching section. The maximum positive dispersion is therefore $\sqrt{\beta_{xC}}\chi_{\max}$, where β_{xC} is the horizontal betatron function at point C . Although this is not a necessary requirement, it is desirable to select this *near- π* insertion as the low-beta insertion because of the following three reasons. First, the low-beta insertion just requires low-beta triplets or doublets so that a length of insertion can be shortened and the lattice would become more compact. Secondly, since the value of χ_{\max} is predetermined by the invariant dispersion action, smaller betatron function at point C would significantly lower the positive dispersion regardless of the type of insertion in the matching section. Thirdly, because of the rapid phase advance and the low value of the betatron function near point C , a small number of dipoles can be introduced here without significantly modifying the shape of the semicircle and increasing the positive contribution to the momentum compaction factor.

On the other hand, if a FODO-cell structure is used for the *near- π* insertion and an F quadrupole is placed at the center, the maximum positive dispersion will be large due to the large value of the betatron function β_{xC} at the F quadrupole. This scheme was used in the design of the main driver of the K factory at TRIUMF [3].

The horizontal dispersion at point A plays an essential role in determining the value of the momentum compaction factor. If the dispersion function has a large enough negative value so that most of the dispersion values in dipoles are negative,

the momentum compaction factor will be negative. However, the maximum value of the dispersion function value of the lattice module is determined by the radius of the circle multiplied by $\sqrt{\beta_{xC}}$, and this needs to be minimized also. A large negative dispersion at point A gives rise to a large dispersion action in the matching section; thus the dispersion function becomes large both positively and negatively. In general, if the dispersion is less negative at point A , the dispersion action in the matching section is also smaller (see Appendix). However, the phase advance required in the matching section decreases creating a larger value of the betatron amplitude function at the symmetry point C . The resulting positive dispersion function at point C becomes larger instead.

2. Choice of F or D Quadrupole at Symmetry Point

From the symmetry point A of Fig. 1, there is a choice to start with the FODO cell or the DOFO cell. In our previous design [7], point A was placed at the center of the D quadrupole from where a DOFO cell started to the right and left, each with a continuation of the quadrupole triplet DFD to provide the low-beta insertion. In the present design of the Main Injector lattice, in order to economize the number of elements, doublets are used in the low-beta insertion instead of triplets. Since it is important to make a large and fast change in the horizontal phase ϕ of the order of π by lowering the horizontal betatron function, the doublet must start from an F quadrupole and be followed by the D quadrupole. If only one cell is used between point A and the doublet, it has to be a FODO cell, or with an F quadrupole at the symmetry point A . However, it is also possible to start from a D quadrupole, if one-and-a-half cells are used. This produces, however, much higher values of the positive dispersion for a given phase advance per cell. A general analytic analysis, presented in the appendix, shows that a basic module beginning with a FODO cell has superior beam dynamics properties.

3. Dependence of γ_t on χ_{\min}

A variation of γ_t is examined with respect to the value of χ_{\min} . The basic module in an example shown below is made of two FODO cells, each of length 27.1600 m, and a symmetrical insertion consisting of two quadrupole doublets. The FODO cells are similar to the FODO cells of the relativistic heavy-ion collider (RHIC) lattice at Brookhaven. There is one dipole of length 9.45 m and bending angle 38.924 mr in each half-FODO cell. There is also a dipole of length 2.953 m and bending angle

12.163 mr located at the center of the symmetric insertion, (the same dipole in the zero-dispersion-suppression cell of the RHIC). The horizontal and vertical phase advances of this module are close to 0.8 ($\nu_x = 0.835$ to 0.76 , $\nu_y = 0.937$ to 0.814) and the module length is close to 72 m. The maximum values of the betatron functions in the FODO cells are for $\beta_x = 52.825$ m and $\beta_y \cong 44.5$ m. Table I shows the dependence of the momentum compaction factor as a function of the initial dispersion function D_{\min} at point A for a lattice example where the horizontal and vertical phase advances in the FODO cells are fixed at 0.181 and 0.295, respectively. For the usual lattice made of the same matched FODO cells only, the dispersion at the F and D quadrupoles are $D_F = 2.529$ m and $D_D = 1.289$ m, respectively. Tables II and III show two more examples with different tunes of the FODO cell, while Table IV shows a module consisting of just three matched FODO cells.

Table I shows that γ_t can be an imaginary number within a range between $i23.275$ up to infinitely large imaginary numbers with the same range in the real domain. While the betatron functions do not change appreciably, the maximum and minimum values of the dispersion function have a wide range from the pair $D_{\min} = -2.5000$ m, $D_{\max} = +0.81343$ m corresponding to $\gamma_t = i23.3$ to the pair $D_{\min} = -0.87700$ m, $D_{\max} = +1.03966$ m corresponding to $\gamma_t = i1007.8$. Figure 2 shows the resulting γ_t values with various χ_{\min} . Each module of the above examples has almost identical length of 72 m and is made of identical magnets. In the fitting procedure all drifts and only one quadrupole length of the doublet were the variables. The only difference between these examples is the minimum of the dispersion function or χ_{\min} .

The momentum compaction factor is plotted against the initial dispersion D_{\min} in Fig. 3. We see a linear relationship except for the three points at the far right which have the highest momentum compaction factors. It is clear from Eq. (1.2) that this linear relationship is exact when the module lengths are constant and when the dipole at the low-beta matching section is absent. The three points that deviate from linearity are found to have module lengths much different from the rest (less than 72 m). In the appendix, this linear relationship is derived analytically with the dipole at the low-beta omitted. The result is presented in Eq. (A10) or (A11), which is shown as dots in Fig. 3. We found that the momentum compaction factors of Table I (except for the three points on the right) agree with the analytical derivation extremely well, if the contribution of the low-beta dipole is removed.

When the starting value of the $\chi_{\min} \approx -0.125$, as is presented in Fig. 2, the momentum compaction factor is very close to zero or γ_t becomes a large imaginary

value (one example is presented in Fig. 2 where $\gamma_t = i104.38$) or a large real value (one case is presented in Fig. 2 where the $\gamma_t = 223.65$). Any small changes of the tunes for these modules will produce a large change in γ_t . The modules where γ_t has large values should not be seriously considered here. However, they are useful in the design of *isochronous* lattices. The module is exactly isochronous when $D_{\min} = -0.885$ m. The analytic formula in the appendix gives the prediction $D_{\min} = -0.660$ m. The discrepancy is again due to the positive contribution of the dipole at the low-beta matching section. Nevertheless, the analytic formula provides a very valuable guide in the design of the modules.

The whole lattice with imaginary γ_t can be easily constructed by using a row of these basic modules. The optical functions of these modules are matched at the symmetry point A , and the number of modules depends only on the geometry of the ring required. A matched straight section with zero dispersion can also be designed by utilizing similar principles.

4. Tune Selection

A choice of the horizontal and vertical betatron tune within the FODO cells is quite different with respect to the regular FODO lattice. One of the important reasons for the choice of the 90° betatron phase for the conventional ring composing of FODO cells is the low value of the dispersion function [4]. Also the lattice will become achromatic for a set of four-FODO-cell combination, where the systematic stopbands are self-canceled. At a lower betatron phase, for example, the 60° cell, the peak value of the dispersion function almost doubles. The momentum-spread contribution to the beam size is directly proportional to the dispersion function while the betatron-oscillation contribution is proportional only to $\sqrt{\beta_x}$ or $\sqrt{\beta_y}$.

The rule [4] for the choice of the phase differences within the FODO cells becomes different in the case of the *modular* imaginary γ_t type of lattice design. The momentum-dispersion values, as it will be shown in an example, can be within the range of $\pm\frac{1}{2}$ of the FODO-cell values by using a smaller phase advance in the FODO cells (see Appendix for analytic analysis). Three modules, made of the same magnetic elements but with different horizontal betatron phases within the FODO cells, were constructed to produce the same value of the imaginary $\gamma_t \sim i45$. The vertical tune within the FODO cells was kept the same at $\nu_y = 0.244$ in these three examples. Figure 4 shows a dependence of the minimum value of the dispersion function on the horizontal betatron tune within the FODO cells. The horizontal tunes in these

examples are $\nu_x = 0.250$, 0.190 , and 0.145 . As these examples show, the module with betatron tune $\nu_x = 0.250$ is no longer preferable compared with the other two modules, because, in order to provide $\gamma_t \approx i45$, the horizontal dispersion ranges from $D_{\min} = -1.82$ m to $D_{\max} = 0.773$ m. If smaller values of the γ_t is required, we need to start this module at a still larger negative dispersion. It appears that the module with horizontal phase advance of $\nu_x = 0.145$ or 52.2° provides a smaller range of dispersion.

Table IV shows that the conventional matched FODO cell with $\nu_x = 0.25$ and $\nu_y = 0.252$ gives rise to the maximum dispersion function at $D_{\max} = 1.428$ m. On the other hand, the example of Table II shows that the dispersion function of the imaginary γ_t module lies within the limit of $D_{\min} = -0.815$ m to $D_{\max} = 0.819$ m with a choice of $\nu_x = 0.142$ in the FODO cell and achieving $\gamma_t = i57.3$. Similarly, the dispersion function of the imaginary γ_t lattice shown in Table III ranges within $D_{\min} = -0.790$ m to $D_{\max} = 0.771$ m, which are 0.56 or 0.54 times the $D_{\max} = 1.428$ m of the regular FODO-cell lattice.

The displacement of the off-momentum particles has opposite signs within most of the dipoles. Particles with higher/lower momenta will travel through the inside/outside parts of the dipoles as represented in Fig. 5.

III. FERMILAB MAIN INJECTOR LATTICE

A complete Main Injector lattice with an imaginary γ_t is constructed with the use of the basic module discussed in the previous section. This design represents a possible alternate solution to the 8 to 150 GeV Main Injector in Fermilab. The transition gamma was selected to be about $\gamma_t = i29.3$ so that the absolute value of the momentum compaction factor would be roughly the same as in the conventional FODO-cell design. This ensures that all collective-instability thresholds would be at least as high as those of the conventional design. The lattice has to follow many geometrical constraints due to the limited site space. It also has to follow the shape of the tunnel of the existing FODO-cell-based design while the total length of the ring measures exactly 3319.4186 m. These constraints were fulfilled. However, the less critical issue of the shape of the tunnel was not completely satisfied. This design uses 300 identical dipoles and tries to recycle as many old Main Ring quadrupoles as possible. There are two long-straight sections with zero dispersion, one of which is reserved for the rf, and six additional straight sections for injection and extraction purposes.

A. Basic Module

The basic module (BASIC) for the latest Fermilab Main Injector imaginary γ_t lattice has twelve dipoles within the two FODO cells (three per half cell) and one dipole in the low-beta insertion. Each FODO cell has a phase advance of 60° . The quadrupoles have a length of 0.988 m. The maximum gradients in the focussing and defocussing quadrupoles in the ring are 220.6 kG/m and -216.8 kG/m, respectively. The maximum values of the horizontal and vertical betatron functions in the FODO cell are 77.39 m and 79.11 m, respectively. The length of the dipoles is 6.096 m given by the prototype magnet already built. The low-beta insertion cell, which is symmetric, joins the two FODO cells together. It consists of two doublets with an almost π phase advance, where the existing quadrupoles from the Fermilab Main Ring are used. The first F quadrupole in each doublet of the insertion shares the same function of the last focussing quadrupole of the FODO cell. This not only eliminates one FODO quadrupole, but also shortens the length of the module, making it more compact. The quadrupoles in the doublet are made of the existing Fermilab Main Ring quadrupoles. The focussing quadrupoles are 2.1336 m and 1.31953 m long while the defocussing quadrupoles are 2.1336 m long. In the central part of the insertion, the horizontal betatron function β_x has a minimum value of 6.54 m at the center, while

the vertical betatron function β_y stays constant at 76.6 m. This arrangement leads to a minimum and maximum of the dispersion function of -2.700 m and $+2.948$ m, respectively. The total length of the basic module is 112.1 m with $\gamma_t = i28.648$. The normalized dispersion function for this basic module has been shown in Fig. 1. The betatron functions and dispersion function are shown in Fig. 6.

B. Extraction-Injection Straights

The extraction-injection straight sections are optimized for the extraction and injection purposes. They consist of essentially two basic modules: one with four missing dipoles in the FODO cells (EXTR1) for the kicker or electrostatic septum devices, and the other with six missing dipoles in the FODO cells (EXTR2) for the magnetic septum devices. The betatron functions within the extraction and injection modules remain almost unchanged except for a slight difference in the positive part of the dispersion function.

The free drift space, where extraction devices such as the magnetic septa would be located, is over 20 m, while the drift length for each electrostatic septum or kicker device for the Main Injector is about 12.5 m. The horizontal betatron tune difference between the septum and the kicker position is $\Delta\nu_x = 0.75$. The values of the horizontal betatron function at the positions of the kicker and magnetic septum are close to the maximum value. This optimizes conditions for injection and extraction. All quadrupoles within the extraction straights are the same as that of the basic module. The lengths of the two modules, which form the injection-extraction straight sections, are 108.5 m and 110.28 m, respectively. Both modules are of imaginary γ_t with values $\gamma_t = i22.21$ and $\gamma_t = i22.66$, respectively. The betatron and dispersion functions of the extraction-injection modules are presented in Fig. 7.

C. Zero-Dispersion Straight

The long zero-dispersion straight section (RFST) is designed with the missing-dipole scheme for zero-dispersion suppression and by using the same technique as for the basic imaginary γ_t module. Figure 8 represents the whole straight section in the normalized dispersion diagram. Again, this module starts from the same point A and follows the path B, C , and curves back to the origin O , where both the dispersion and the slope of the dispersion function are equal to zero. There are three dipoles in the low-beta insertion and Fig. 8 shows that as expected they do not change the circular shape of the normalized dispersion function. It is clear that point B in this module is

much closer to the origin because of the two missing dipoles at the end of the FODO cell. At the origin O , there is a long rf straight section with the zero dispersion — presented this time only as a point at the origin. To obtain the zero-dispersion straight, it is necessary to bring the normalized dispersion function from point A to the origin O via points B and C . The last dipole in the zero-dispersion-suppression cell should be placed close to the ξ axis at the negative side so that its end would be at the origin O . Figure 8 also shows that the two missing dipoles at the end of the FODO cell are necessary to provide for smaller radius of the closure circle. It is important to note that the same method has been successfully used at Fermilab for beam line matching designs [9]. The total length of a dispersion-free FODO cell is 80 m, which is available for the rf stations, while the length of the whole zero-dispersion module, with the zero-dispersion-suppression cells on both sides, is 329.22 m. This module itself has a real value for the transition energy, or $\gamma_t = 41.15$. The betatron and dispersion functions in this RFST module with zero dispersion are presented in Fig. 9. The quadrupoles in RFST dispersion-free modules are identical to the basic module except that the length of one of the quadrupoles should be 2.0443 m, which is 4.19% shorter than that of the standard 2.1336 m quadrupole. The old Main Ring 2.1336 m quadrupole equipped with a shunt can be a satisfactory substitute.

All betatron functions and dispersion functions between the modules are perfectly matched at point A . Each module is also matched to a module of the same kind. The whole ring has twofold symmetry and is defined as 2[RFST, (EXTR1, EXTR2), 5(BASIC), (EXTR2, EXTR1), BASIC, (EXTR2, EXTR1)]. These two dispersion free straight sections can be used for spin rotators (snakes) for maintaining spin polarization during polarized-proton acceleration. There are altogether 300 dipoles in this lattice and they are all of the same type.

Properties of this imaginary γ_t lattice can be summarized as following.

$$\begin{aligned}
&\text{circumference } C = 3319.4186 \text{ m} , \\
&\text{horizontal tune } \nu_x = 21.4197 , \\
&\text{vertical tune } \nu_y = 11.1905 , \\
&\text{transition gamma } \gamma_t = i29.3 , \\
&\text{maximum horizontal beta } \hat{\beta}_x = 78 \text{ m} , \\
&\text{maximum vertical beta } \hat{\beta}_y = 79 \text{ m} .
\end{aligned}$$

IV. BEAM DYNAMICS OF THE MAIN INJECTOR LATTICE

A lattice with properly matched betatron functions does not necessarily represent an acceptable solution. Properties such as (1) chromatic correction and perturbations, (2) sensitivity to errors, (3) tunability, (4) dynamical aperture, (5) spin-depolarizing resonance strength, etc. are also important. In this section, we shall examine these lattice properties for the Main Injector lattice.

A. Dependence on Momentum

The natural chromaticities of this imaginary γ_t example are, respectively,

$$\xi_x = \frac{d\nu_x}{d\delta} = -39.18 \quad \text{and} \quad \xi_y = \frac{d\nu_y}{d\delta} = -19.98, \quad (4.1)$$

where $\delta = \Delta p/p_0$. The horizontal and vertical betatron base tunes are $\nu_x = 21.42$ and $\nu_y = 11.19$, respectively. The chromaticity correction sextupoles consist of one SEXH, two SEX1's, and two SEXV's for each of the 24 modules except for the dispersion-free ones. The SEXH's are located at the FODO F quadrupoles where the horizontal dispersion has the negative value of -2.6 m and $\beta_x \approx 72.8$ m, $\beta_y \approx 30.2$ m. The SEX1's are located at the F quadrupoles of the doublets where the dispersion is $+1.8$ m and $\beta_x \approx 72.8$ m, $\beta_y \approx 30.2$ m. The SEXV's are located at the D quadrupoles of the doublets where the dispersion is $+1.5$ m and $\beta_x \approx 11.4$ m, $\beta_y \approx 79.5$ m. The integrated strengths of the sextupoles ($B''\ell/B\rho$) to compensate for the natural chromaticities are found to be $k_{sf} = -0.0565 \text{ m}^{-2}$ for the SEXH's, $-k_{sf}$ for the SEX1's, and $k_{sd} = -0.104 \text{ m}^{-2}$ for the SEXV's. This means that there are only two power supplies, one bus for the SEXH's and SEX1's and the other bus for the SEXV's. The available drifts for the SEXH's, SEX1's, and SEXV's are 1.5 m, 0.84 m, and 1.348 m, respectively. Because the chromaticities do not change sign during the acceleration cycle, lengths of 0.4 m for the SEXH and SEX1, and 0.5 m for the SEXV sextupoles will be quite adequate.

The dependences of betatron functions on momentum of the chromaticity-compensated lattice were examined first. Two computer programs, the SYNCH and the MAD, were used to study the chromatic properties up to $\Delta p/p_0 = \pm 1.5\%$, although the estimated momentum spread in the future Main Injector should be less than $\pm 0.2\%$. Table V shows that the off-momentum closed orbit, the maxima of $\sqrt{\beta_x}$ and $\sqrt{\beta_y}$ functions, and dispersion functions do not depend significantly on momentum. Figure 10 shows the dependences of the maximum relative deviations of

betatron functions on momentum deviation. Figure 11 shows the dependences of maximum and minimum dispersion on momentum deviation.

We have demonstrated that chromatic properties of the imaginary γ_t lattice are at least comparable to that of the FODO lattice. The maximum of the positive and negative values of the dispersion function in the imaginary γ_t lattice can be designed equal to $\frac{2}{3}$ or even $\frac{1}{2}$ of the maximum value of the dispersion function of a conventional FODO lattice, as shown in Table I. Table VI shows another example to compare the maximum dispersion functions for the conventional FODO cells at $\nu_x = 0.250$ and $\nu_y = 0.252$ with that of similar imaginary basic modules at different initial negative dispersion functions and resulting γ_t values. Note here that the maximum dispersion function is greatly reduced when the phase advance of the FODO cell in the basic module is around 60° . The magnitude of the dispersion function is however a trade-off between the dispersion function and the magnitude of the momentum compaction factor. Due to a smaller maximum dispersion function for the imaginary γ_t lattices, the momentum aperture requirement is reduced. The corresponding dynamical aperture will be enhanced.

B. Chromaticity and Distortion Function Analysis

The chromaticity sextupoles represent the main source of nonlinearities. The imaginary γ_t lattice belongs to the group of lattices where a high focussing is used to provide low emittance and high brilliance in the new generation synchrotron light sources. The large natural chromaticity requires strong sextupole chromaticity compensation. This produces larger amplitude distortions or second-order-sextupole-induced tunes shifts with amplitude.

The amplitude dependence of tunes shifts due to sextupoles (detuning) can be written as:

$$\begin{aligned}\Delta\nu_x &= a \epsilon_x / \pi + b \epsilon_y / \pi , \\ \Delta\nu_y &= b \epsilon_x / \pi + c \epsilon_y / \pi ,\end{aligned}\tag{4.2}$$

where ϵ_x and ϵ_y are the horizontal and vertical emittances, defined as amplitude squared divided by the betatron function. The detunings are [13]

$$\begin{aligned}a &= -\frac{1}{8\pi} \sum_k (B_3 S + 3B_1 \bar{S})_k , \\ b &= -\frac{1}{4\pi} \sum_k (B_+ \bar{S} + B_- \bar{S} - 2B_1 \bar{S})_k ,\end{aligned}$$

$$c = -\frac{1}{8\pi} \sum_k (B_+ \bar{S} - B_- \bar{S} + 4\bar{B} \bar{S})_k . \quad (4.3)$$

Here, the reduced sextupole strengths are

$$S_k = \left(\frac{B''\ell}{B\rho} \beta_x^{3/2} \right)_k \quad \text{and} \quad \bar{S}_k = \left(\frac{B''\ell}{B\rho} \beta_x^{1/2} \beta_y \right)_k , \quad (4.4)$$

evaluated at position k of the sextupole having a length $\ell \rightarrow 0$. The distortion functions B_1 , B_3 , \bar{B} , B_\pm at location k are defined as [14]:

$$B_{1k} = \frac{1}{16 \sin \pi \nu_x} \sum_{k'} S_{k'} \cos(|\psi_{xk'} - \psi_{xk}| - \pi \nu_x) , \quad (4.5)$$

$$B_{3k} = \frac{1}{16 \sin 3\pi \nu_x} \sum_{k'} S_{k'} \cos(3|\psi_{xk'} - \psi_{xk}| - 3\pi \nu_x) , \quad (4.6)$$

$$\bar{B}_k = \frac{1}{16 \sin \pi \nu_x} \sum_{k'} \bar{S}_{k'} \cos(|\psi_{xk'} - \psi_{xk}| - \pi \nu_x) , \quad (4.7)$$

$$B_{\pm k} = \frac{1}{16 \sin \pi \nu_\pm} \sum_{k'} \bar{S}_{k'} \cos[2|\psi_{yk'} - \psi_{yk}| \pm |\psi_{xk'} - \psi_{xk}| - \pi \nu_\pm] , \quad (4.8)$$

where $\nu_{x,y}$ are the horizontal and vertical base tunes of the ring and $\nu_\pm = 2\nu_y \pm \nu_x$.

The nonlinearity can be minimized by lowering the detunings or tuneshift-dependences on amplitude. One way to accomplish this is to minimize the distortion functions. The first thing to do is to minimize the strengths of the sextupoles by placing them at the most advantageous positions. This imaginary γ_t lattice contains a lot of low-beta insertions. The quadrupoles in the low-beta doublets are much stronger than the FODO quadrupoles and they are significant contributors to the chromaticities. In order to provide local chromaticity compensation with low-power sextupoles, these sextupoles must be placed as close to the low-beta doublets as possible. We follow this guideline and place one sextupole (SEX1) in front and another sextupole (SEXV) after the low-beta doublet. In this way the strengths of the two sextupole buses required for chromaticity correction come out to be as low as $k_{sf} = \mp 0.0565 \text{ m}^{-2}$ for SEXH and SEX1 and $k_{sd} = -0.104 \text{ m}^{-2}$ for SEXV. These strengths correspond to pole-tip fields of 1.77 and 3.25 kG, respectively, at 150 GeV for sextupoles of length 20 cm and aperture radius 5 cm.

From Eqs. (4.5) to (4.8), it is easy to see that the distortion functions B_1 , B_3 , \bar{B} , and B_\pm are actually cosine projections of the vectors \mathbf{B}_1 , \mathbf{B}_3 , $\bar{\mathbf{B}}$, and \mathbf{B}_\pm which rotate with phase angles ψ_x , $3\psi_x$, ψ_x , and $2\psi_y \pm \psi_x$. On passing through a thin sextupole at location k , the cosine projections of the vectors remain continuous while the sine

projections jump by either $\frac{1}{8}S_k$ or $\frac{1}{8}\bar{S}_k$. Therefore, the sufficient conditions for the five distortion functions to vanish at a location can be written simply as:

$$\sum_{k'} S_{k'} e^{i\psi_{xk'}} = 0 , \quad (4.9)$$

$$\sum_{k'} S_{k'} e^{i3\psi_{xk'}} = 0 , \quad (4.10)$$

$$\sum_{k'} \bar{S}_{k'} e^{i\psi_{xk'}} = 0 , \quad (4.11)$$

$$\sum_{k'} \bar{S}_{k'} e^{i\psi_{\pm k'}} = 0 , \quad (4.12)$$

where the summation is over all sextupoles k' , whose phase angles $\psi_{xk'}$, $\psi_{yk'}$, and $\psi_{\pm k'} = 2\psi_{yk'} \pm \psi_{xk'}$ are measured *downstream* of the point of consideration. For a FODO-cell ring, the above conditions can be easily satisfied by choosing the phase advance per cell to be either 60° or 90° in both transverse planes. Such an idea can also be extended to our non-FODO ring. This ring has two superperiods. Between the two special zero-dispersion modules, there are 12 modules on each side, which consists of [(EXTR1, EXTR2), 5(BASIC), (EXTR2, EXTR1), BASIC, (EXTR2, EXTR1)]. Although there are three types of modules here, their Courant-Snyder parameters are similar. In the design, the horizontal and vertical phase advances for each of these three types of modules were chosen to be as close as possible to 270° (0.75) and $270^\circ/2$ (0.75/2), respectively. Thus, the distortion functions B_1 , B_3 , and \bar{B} will be *canceled* for every four modules downstream. The phase advances of the modules were selected as listed in Table VII.

Take B_1 as an example. The contributions of the five sextupoles in a BASIC module as indicated in Fig. 12 give a vector of amplitude of $42.9 \text{ m}^{-1/2}$ according to Eq. (4.9) or a B_1 of maximum value $2.76 \text{ m}^{-1/2}$ according to Eq. (4.5). The average phase advance per module is $\Delta\psi_x/2\pi = 0.747$. Therefore, the cancellation is every four adjacent modules among the twelve that contain sextupoles. In fact, the cancellation is more than that. For every four adjacent modules, the first one is canceled by the third and the second by the fourth. If the point of consideration is inside the first (fourth) module, contribution should come from only the first (second) and the third (fourth) modules. If the point of consideration is inside the second or third module, however, contribution will come from all the four modules. Fortunately,

the horizontal tune of the ring $\nu_x = 21.4197$ is not far from a half-integer, the vectors of neighboring modules in the summation in Eq. (4.8) will always be about 90° apart independent of whether one is downstream or upstream relative to the other. For example, if the point of consideration is at the end of the second module or the beginning of the third module, the contributions of the first and third modules are almost in the same direction, orthogonal to which are the contributions of the second and fourth modules. Therefore B_1 can have an amplitude of $2.76 \times 2\sqrt{2}$ or $7.8 \text{ m}^{-1/2}$. At this location, the projection cosine is about $\frac{1}{\sqrt{2}}$ giving $B_1 \approx 5.5 \text{ m}^{-1/2}$.

Figure 13 shows a plot of B_1 for half of the ring starting from the middle of the dispersionless rf straight. Since there is no sextupole in the rf straight, we see B_1 oscillates sinusoidally according to the horizontal phase ψ_x just like the betatron oscillation. Since the cancellation has not been perfect, B_1 is different from zero here. In fact, the average phase advance per module is $\Delta\psi_x/2\pi = 0.7472$. Adding up the 12 modules, we get instead of zero,

$$\left| \frac{1 - e^{i12\Delta\psi_x}}{1 - e^{i\Delta\psi_x}} \right| = \left| \frac{\sin 6\Delta\psi_x}{\sin \frac{1}{2}\Delta\psi_x} \right| = 0.148 . \quad (4.13)$$

Thus, we expect the imperfect cancellation gives $B_1 = 2.96 \times 0.148 \text{ m}^{-1/2} = 0.44 \text{ m}^{-1/2}$ for 12 modules. The other 12 modules give the same contribution but is separated by a phase of $\pi\nu_x$ or 104.45° . Thus the total contribution amounts to $0.54 \text{ m}^{-1/2}$, which is to be compared with $0.40 \text{ m}^{-1/2}$ in the plot of Fig. 13. At $\psi_x/2\pi = 0.88$, we meet with the SEXH of the first of the 12 sextupole-loaded modules, and see B_1 bend over at an angle. Very soon, we are at the low-beta (centered at $\psi_x/2\pi = 1.24$), and the phase jumps rapidly showing a gap on the plot. The second module starts from $\psi_x/2\pi = 1.61$ and has the low-beta phase-jump gap centered at $\psi_x/2\pi = 1.98$. We reach the end of the second module at $\psi_x/2\pi \sim 2.36$, which is one of the points of consideration discussed in the previous paragraph. We see that B_1 reaches a maximum of $6.2 \text{ m}^{-1/2}$, which is quite close to our crude estimation of $5.5 \text{ m}^{-1/2}$. We also see that B_1 repeats itself every 4 modules as expected.

The distortion function \bar{B} rotates with ψ_x . We therefore expect it to behave exactly the same as B_1 . However, the sine projection of the vector $\bar{\mathbf{B}}$ jumps by $\frac{1}{2}\bar{S}$ instead when passing through a sextupole. As a result, the vectors for the 5 sextupoles in module BASIC are different. As is shown in Fig. 14, the amplitude of vector sum of $\bar{\mathbf{B}}$ is only 12.7, which is only 30% of that for B_1 . The plot of \bar{B} in Fig. 15 does show a maximum of only $2.3 \text{ m}^{-1/2}$ inside a group of 4 modules. In the rf straight, however, the maximum \bar{B} is $0.37 \text{ m}^{-1/2}$ which is *not* 30% of B_1 . The vector sum in Fig. 14

is small because of the large vectorial cancellation between the 5 sextupoles. This implies that the vector sum may differ by very much for different types of modules. In fact, for modules EXTR1 and EXTR2, the vector sums have amplitudes 14.3 and 13.6 $\text{m}^{-1/2}$ instead, which are 12% and 6% larger than those for module BASIC. On the other hand, the largest difference for the vector sum is only 2.4% for B_1 . This explains the large value of \bar{B} in the rf straight.

The vector \mathbf{B}_3 rotates according to $3\psi_x$, which is the main difference from \mathbf{B}_1 and $\bar{\mathbf{B}}$. The vector plot of \mathbf{B}_3 for the BASIC module is shown in Fig. 16 and the plot of B_3 in Fig. 17. We see that B_3 reaches a maximum of 17.9 $\text{m}^{-1/2}$ inside a group of 4 modules and 2.7 $\text{m}^{-1/2}$ in the rf straight. These values are considerably larger than those for B_1 . First, the vectorial sum for a module adds more constructively giving an amplitude of 61.9 $\text{m}^{-1/2}$, which is 1.44 times that for B_1 . Second, the $\sin 3\pi\nu_x$ in the numerator of Eq. (4.6) gives a factor 1.33 larger than the $\sin \pi\nu_x$ in B_1 . Since the phase advance per module is now $3\Delta\psi_x = 2.2416$, the cancellation of the 12 modules will be worse; the factor in Eq. (4.13) becomes 0.445 instead of 3.0 times larger. Therefore, in the rf straight, $(B_3)_{\max} \approx (B_1)_{\max} \times 1.44 \times 1.33 \times 3.0 = 2.3 \text{ m}^{-1/2}$, to be compared with 2.7 $\text{m}^{-1/2}$ in Fig. 17.

The value of B_3 inside a group of 4 modules can also be explained. Since $3\nu_x = 64.2591$, the adjacent module upstream will have a relative phase of $3(\nu_x - \Delta\psi_x/2\pi) = 62.0175$. Thus for a point of consideration at the end of the second module and the beginning of the third, the relative phases for the four modules contributing to the summation of Eq. (4.10) will be, respectively, 59.77, 62.01, 0.00, and 2.24. In other words, the first module cancels the fourth and the contributions of the second and the third are nearly the same. Using the vector sum of 61.9 $\text{m}^{-1/2}$ in Fig. 16 and Eq. (4.6), we obtain a value of 13.3 $\text{m}^{-1/2}$ for B_3 , where we have added the 2.7 $\text{m}^{-1/2}$ we computed for the imperfection of cancellation of the whole ring. This is to be compared with the $\sim 14 \text{ m}^{-1/2}$ of Fig. 17 at $\psi_x/2\pi = 2.36$. As is indicated in the figure, $(B_3)_{\max} = 17.9 \text{ m}^{-1/2}$ actually occurs before this point inside the low-beta insertion of the second module, which can also be estimated.

The story is slightly different for the distortion function B_+ . Here, the average phase advance per module is $\Delta\psi_+ = 2\Delta\psi_y + \Delta\psi_x = 1.49$. Thus, there will be cancellation for every two adjacent modules instead. In other words, the largest contribution to B_+ comes from only two modules. For this reason, although the summation in Eq. (4.12) adds up to a vector of amplitude 29.5 $\text{m}^{-1/2}$ for one module (Fig. 18), B_+ has a maximum of only 2.2 $\text{m}^{-1/2}$ (Fig. 19). We observe that B_+ has an

unusually large amplitude of $2.0 \text{ m}^{-1/2}$. This is because $\Delta\psi_+/2\pi = 1.4554$ for module EXTR1 which is far from 180° . Also the vector sums for the 3 types of modules differ by 12%. All these lead to the imperfect cancellation among the 12 modules.

The distortion function B_- rotates with a tune of $\nu_- = 2\nu_y - \nu_x = 0.9612$ which is extremely slow. Therefore, cancellation between adjacent modules will not be possible. In the present arrangement, it also turns out that there is no cancellation among the five sextupoles within a module. However, due to the near integral value of ν_- and the two-fold symmetry of the ring, each sextupole in the first 12 modules is *almost* canceled by a complementary sextupole in the other 12 modules. Exact cancellation will occur if ν_- is exactly an integer. But this is not desirable since the performance will be exactly at a difference resonance. In our lattice, each module contributes a vector of length $\sim 24 \text{ m}^{-1/2}$ (Fig. 20) to the summation in Eq. (4.12) and, together with its complementary module on the other side of the ring, contributes a vector of length $\sim 24 \times 2 \cos \frac{1}{2}\pi\nu_- \approx 2.9 \text{ m}^{-1/2}$. Each of the 12 adjacent modules has almost the same phase advance $2\psi_y - \psi_x$. Therefore, from Eq. (4.8), $|B_-|$ may reach the maximum value of

$$|B_-|_{\max} \approx 12 \times \frac{24 \times 2 \cos \frac{1}{2}\pi\nu_-}{16 \sin \pi\nu_-} = \frac{18}{\sin \frac{1}{2}\pi\nu_-} \approx 18 \text{ m}^{-1/2}, \quad (4.14)$$

which agrees well with the actual numerical computation plotted in Fig. 21. Note that this value is insensitive to how close the difference resonance is.

Going through a low-beta insertion, ψ_x advances much faster than ψ_y so that ψ_- actually decreases across the insertion. In the plot of B_- versus ψ_- in Fig. 21, we see that B_- starts from $\sim -18 \text{ m}^{-1/2}$ at the center of the rf straight and increases to $\sim 18 \text{ m}^{-1/2}$ near the first low-beta doublet of the first module. Then the phase ψ_- suddenly goes back to near zero and B_- drops to $\sim -14 \text{ m}^{-1/2}$ while crossing the low-beta region. Then, both $\psi_-/2\pi$ and B_- advance again reaching 0.25 and almost zero, respectively, when the SEXH of the next module is reached. The phase advance per module is $\Delta\psi_-/2\pi = -0.005$, so that each module has roughly the same ψ_- and the plot of B_- has the shape of a butterfly.

With this arrangement of sextupoles, the nonlinearity of the chromaticity sextupoles mostly cancels. From MAD and SYNCH, the tunes shift dependences on amplitude were calculated to be

$$\begin{aligned} \nu_x &= 21.41970 - 97.2\epsilon_x/\pi - 40.5\epsilon_y/\pi, \\ \nu_y &= 11.19045 - 40.5\epsilon_x/\pi + 1.22\epsilon_y/\pi, \end{aligned} \quad (4.15)$$

where the emittances ϵ_x and ϵ_y are in m. The detunings here are actually smaller than those of the existing FODO lattice of the Fermilab Main Injector by 50%. As a result, harmonic sextupoles are not required. In our previous design of the same imaginary γ_t lattice [7], these special precautions had not been taken, and the detunings [defined in Eq. (4.2)] turned out to be

$$a = 4.82 \times 10^2 \text{ m}^{-1}, \quad b = -1.56 \times 10^4 \text{ m}^{-1}, \quad c = -7.49 \times 10^3 \text{ m}^{-1}. \quad (4.16)$$

which are very large. In order to maintain a reasonably large amplitude, a family of harmonic sextupoles was installed in the previous lattice to lower the nonlinearity; the three detunings then reduced to 4.43×10^2 , -2.81×10^2 , and $1.33 \times 10^3 \text{ m}^{-1}$, which are still much larger than the detunings of the present design as given in Eq. (4.15).

C. Half-Integer Stopbands and Betatron Beatings

The horizontal or vertical off-momentum betatron beating amplitude [1] can be calculated according to

$$\frac{\Delta\beta(s)}{\beta(s)} = \frac{1}{2\sin(2\pi\nu_0)} \oint ds' \Delta K(s') \beta(s') \cos[2|\psi(s) - \psi(s')| - 2\pi\nu_0], \quad (4.17)$$

where ΔK is the gradient error, β is the betatron amplitude function, ψ is the betatron phase, and ν_0 is the unperturbed or base betatron tune of the accelerator ring. In terms of the phase

$$\phi(s) = \frac{\psi(s)}{\nu_0} = \int_0^s \frac{ds}{\nu_0\beta}, \quad (4.18)$$

which ranges from zero to 2π around one turn of the ring, and the integral

$$J_p = \oint ds \beta(s) \Delta K(s) e^{-ip\phi(s)}, \quad (4.19)$$

Eq. (4.18) can be Fourier expanded as

$$\frac{\Delta\beta(s)}{\beta(s)} = -\frac{\nu_0}{\pi} \sum_{p=-\infty}^{\infty} \frac{J_p e^{ip\phi(s)}}{4\nu_0^2 - p^2}. \quad (4.20)$$

We see that the above sum diverges when the tune is a half-integer. In fact, a lattice will be linearly unstable in a region where the tune is near to a half-integer. The stopband is given by $\delta\nu_0 = |J_p|/2\pi$ where $p = 2\nu_0$. For a systematic half-integer resonance, the gradient error is given by

$$\Delta K(s) = -K\delta + \frac{B''}{B\rho}D\delta + \dots, \quad (4.21)$$

where the first term is the variation of the quadrupole gradient due to momentum offset and the second term is the feed-down contribution from the sextupoles.

Now, if the modules in our lattice are identical, each with a phase advance of $2\pi\nu$, the systematic stopband integral becomes

$$J_p = J_p^\circ \left\{ 1 + e^{-i2\pi p\nu/\nu_0} + e^{-i4\pi p\nu/\nu_0} + \dots \right\}, \quad (4.22)$$

where J_p° is the stopband integral for the first module, while the second and third terms inside the curly brackets are contributions from the second and third modules. For a module of phase advance 90° or an odd multiple of 90° , it is clear that the systematic stopband integral for adjacent modules will cancel each other at the harmonic $p \approx 2\nu_0$. Similarly, if the phase advance of each module is 60° , the vector sum of three adjacent modules will cancel each other.

As will be shown in the appendix for an imaginary γ_t lattice with a FODO cell, the phase advance of a basic module (similarly for other modules) will be $\frac{3}{4}\pi$ for a properly chosen initial dispersion value and the phase advance of the FODO cell. Thus, the stopband integral cancels for two adjacent modules. This is the concept of the half-integer stopband-compensation scheme [11, 12] which was usually used for large colliders like RHIC, LEP, etc. In the case of smaller rings, such as synchrotron light sources, additional families of sextupoles were introduced. As was reported in Sec. IV A, the betatron function dependence on momentum of the chromaticity compensated lattice was too small to be seriously taken into consideration especially within the expected momentum range $\pm 0.2\%$. The betatron beating due to momentum for this lattice at the particle momentum offset of $\pm 0.2\%$ was less than 1%. The cancellation of systematic stopband width plays an important role in the tunability of the lattice, where the betatron tune can be adjusted without distorting the betatron amplitudes.

D. Tunability of the Lattice

For a flexible lattice, the betatron tune should be adjustable to within ± 1 unit without much impact on the performance. For the present lattice, the horizontal (vertical) tune was varied for ± 2 units while the vertical (horizontal) tune was kept constant. The starting tunes were $\nu_x = 21.42$ and $\nu_y = 11.19$. The results from the study of the betatron function dependence on the horizontal tune are presented

in Fig. 22. When the horizontal tune is away from the integer and in the region of $\nu_x > 21.1$ and $\nu_x < 21.8$, the horizontal beam size ($\sqrt{\beta_x}$) does not change by more than 2%. If the horizontal tune is lowered to the region $20.5 < \nu_x < 20.9$ or raised to the region $22.1 < \nu_x < 22.6$, the horizontal beam size ($\sqrt{\beta_x}$) does not change by more than 10%. The vertical beam size remains within a range of $\pm 2\%$ when the horizontal tune ν_x changes within a range of ± 1.5 units.

The beam-size dependence on the vertical tune is shown in Fig. 23. The vertical beam size does not change by more than 2% if the vertical tune avoids the integer values and is within the region of $11.05 < \nu_y < 11.55$. When the vertical tune is lowered from the operating tune of 11.2 down to $10.4 < \nu_y < 10.95$, the vertical beam size $\sqrt{\beta_y}$ increases up to 8%. The vertical beam size is above 18% when the vertical tune is above 12. The horizontal beam size $\sqrt{\beta_x}$ remains less than 1% for the vertical tune range of $10 < \nu_x < 12.5$.

The designed lattice with imaginary γ_t , as well as the present Main Injector design based on the conventional FODO-cell structure, has twofold symmetry due to some special injection and extraction constraints. The integer-tune resonance of the betatron functions in the ring with the two-fold symmetry is to be expected [16]. (The systematic half-integer resonance in the accelerator with N superperiods are located at $\nu = \frac{1}{2}N, N, \frac{3}{2}N, \dots$.) The horizontal dispersion showed a similar dependence on the horizontal tune as the horizontal betatron function. The dispersion function becomes large when the horizontal tune reaches the integer values [1]. This is expected, because the dispersion at location s is given by

$$D_x(s) = \frac{1}{2 \sin \pi \nu_x} \oint ds \frac{\sqrt{\beta_x(s)\beta_x(s')}}{\rho(s')} \cos[\pi \nu_x - |\phi_x(s) - \phi_x(s')|] . \quad (4.23)$$

All these results were obtained from SYNCH program calculations. It is possible to change the tunes by ± 1 unit without noticeable changes in all betatron functions if the integer tunes are avoided.

E. Misalignment Errors

It is impossible to align all beam elements perfectly. Transverse misalignment errors can lead to offsets of the closed orbit, which must be corrected during operation. If all the misalignments are random, uncorrelated, and have a variance $\langle z^2 \rangle$ where $z = x$ or y , it is easy to show that the closed-orbit offset $z_{co}(s)$ at location s has a variance given by

$$\langle z_{\text{co}}^2(s) \rangle = \langle z^2 \rangle \frac{\beta_z(s)}{2 \sin \pi \nu_z} \sum_i \left(\frac{B' \ell}{B \rho} \right)_i \beta_{zi} \cos[\pi \nu_z - |\psi_{zi} - \psi_z(s)|] . \quad (4.24)$$

In the above B' is the field gradient of the quadrupole and ℓ its length, the summation runs over all the quadrupoles in the lattice, and the thin-lens approximation has been assumed. The computation was performed by reading a SYNCH output file, the $\langle z_{\text{co}}^2(s) \rangle$'s were computed at each quadrupole, and the maxima were recorded. We obtained the misalignment sensitivity factors:

$$S_z = \left[\frac{\langle z_{\text{co}}^2(s) \rangle}{\langle z^2 \rangle} \right]_{\text{max}}^{\frac{1}{2}} = \begin{cases} 24.6 & \text{horizontal} \\ 48.6 & \text{vertical} \end{cases} \quad (4.25)$$

Since S_z follows a Rayleigh distribution, there is a 98% probability that the closed-orbit offset will fall within $2S_z$. The sensitivity factors are about a factor of two less than those for the previous imaginary γ_t design [7]. There, the middle quadrupoles in the low-beta-insertion triplets are over 4 m in length and these quadrupoles alone contribute about 90% to the sensitivity factors. In our present design, only doublets are used in the low-beta insertions. In order to recycle old Main Ring quadrupoles, the focussing quadrupoles are composed of two pieces, 2.1336 m and 1.31953 m long, while the defocusing quadrupoles are 2.1336 m long. The weaker quadrupole strengths and the smaller number of quadrupoles reduced significantly the misalignment sensitivity factors.

F. Dynamical Aperture Study

The dynamical aperture was studied with multiturn tracking using the TEAPOT program [17]. The dipole multipoles in the ± 25.4 mm range were provided from the magnetic measurements of the Main Injector prototype dipoles. The vertical magnetic field in the plane of the ideal orbit has the harmonic expansion

$$B_z + iB_x = B_0 \sum_{n=0}^{\infty} (b_n + ia_n)(x + iy)^n , \quad (4.26)$$

where B_0 is the vertical bending field at the ideal orbit, b_n 's ($b_0 = 1$) are called the normal multipole coefficients, and a_n 's are skew multipole coefficients, which we ignore in this analysis. Since the dipoles are not superconducting, only systematic errors are included, because random errors are supposed to be small, though not necessarily true in all cases.

The magnetic-field measurements were accurate up to the distances of 25.4 mm. At the injection energy of 8.9 GeV, the sextupole in the dipoles was positive with $b_2 = 0.0654 \text{ m}^{-2}$ while the decapole contribution was $b_4 = 4.27 \text{ m}^{-4}$. The multipoles were placed in the center of the dipoles as thin lenses. A particle was launched at the center of the dispersionless rf straight with a certain horizontal displacement x . The vertical displacement y was varied and the maximum recorded for a survival of 35,000 turns or approximately 0.38 sec of the injection. The initial angular displacements x' and y' were set at zero in all cases. Sometimes the initial y displacement was fixed while the x displacement was varied instead. In this way we scanned the whole x - y space and obtained the aperture plot shown in Fig. 24. The tracking had been done for particles with momentum offsets of 0.2% and 1.0%. Due to the small detunings presented in Eq. (4.15), the aperture turns out to be fairly large. Even at a momentum offset of 1.0%, the allowable normalized emittance is larger than $200\pi \text{ mm-mr}$ in both planes, while the required aperture is only $40\pi \text{ mm-mr}$.

The lattice was next tracked at 19 GeV when the eddy currents are supposed to have a maximum; the corresponding multipoles at 25.4 mm are: $b_2 = 0.561 \text{ m}^{-2}$, $b_4 = 23.23 \text{ m}^{-4}$, and $b_6 = 6677 \text{ m}^{-6}$. The 35,000-turn survival apertures for 0.2% and 1.0% momentum offsets are shown in Fig. 25. Here the allowable normalized emittances are $200\pi \text{ mm-mr}$ and $500\pi \text{ mm-mr}$ in the horizontal and vertical planes, respectively.

We should point out that the apertures shown in both plots are not necessarily real. This is because the magnetic field was not presented correctly at distances over 25.4 mm. Also the chromaticity sextupole settings for the tracking have been designed for complete chromaticity compensation. When the ring runs at chromaticities different from zero, the sextupole strengths will be different, and the aperture will be affected. Also synchrotron oscillation had not been included in the tracking. Nevertheless, results from the Main Injector lattice presented in Figs. 24 and 25 illustrate that large apertures can be achieved in imaginary γ_t lattice.

V. CONCLUSION

In conclusion, we have reviewed methods of designing an accelerator or storage ring lattice with imaginary γ_t . Analytic formulas as well as numerical examples have been used to demonstrate the basic design principle of the imaginary γ_t lattice, where the basic imaginary γ_t modular structure has been exploited for easy construction. A basic module of the imaginary γ_t lattice is made of two FODO cells matched by a reflective symmetric doublet-matching section. Analytic analysis and numerical examples indicate that the dispersion and betatron amplitude matching can be achieved easily.

We also proved analytically (in Appendix) that the phase advance of the module is determined by two parameters, the phase advance per cell in the FODO cell and the initial dispersion function at the focusing quadrupole. The magnitude of the momentum compaction factor is determined in turn by the initial dispersion value. With a proper choice of the dispersion value, the maximum betatron functions and the maximum dispersion function are comparable with the similar lattice with FODO cells alone. With a proper choice of the phase advance in each module, the half-integer and third-order stopband widths can be minimized with excellent chromatic properties. We have also studied *analytically* the chromatic distortion functions due to chromatic sextupoles and demonstrated that excellent distortion function cancellation can be achieved without resorting to extra families of sextupoles. Therefore, the dynamical aperture achieved in the present imaginary γ_t lattice is at least as large as that of the regular FODO cell lattice.

A completed Fermilab Main Injector lattice has been used to demonstrate the design principle. A zero-dispersion section can be constructed using the same principle. The tunability of the lattice is found to be excellent due to the smallness of the systematic half-integer stopband. The tune can be changed without greatly exciting the $[2\nu]$ harmonics. Thus, the betatron-function distortion can be minimized when the betatron tunes are changed.

A major advantage of the imaginary γ_t lattice is that transition crossing is avoided. Because the momentum compaction factor is negative, the longitudinal motion of beam particles is always below transition where the space-charge impedance does not cause microwave instability. The longitudinal phase space blowup and possible beam loss due to nonlinear synchrotron motion around the transition energy region can be avoided. It is important to note that the desired value of γ_t could be adjusted during the design procedure because the γ_t value depends on the average value of the

dispersion function through the dipoles.

With the present design concept, there is no need for the dipoles with an opposite bend angle [18] to cancel out the longer (shorter) path length of the higher- (lower-) momentum particles as in the regular FODO structure. In the imaginary γ_t lattice, the horizontal offsets and their slopes at the dipoles were designed to provide for this cancellation.

Applying the imaginary γ_t design principle, a lattice with zero momentum compaction factor, or the *isochronous* storage ring, can be designed by a proper choice of the dispersion function. Combining the choice of the phase advances per FODO cell, an isochronous storage ring can also be designed with excellent beam dynamics properties.

APPENDIX: THE BASIC MODULE

The basic module of an accelerator lattice is usually made of FODO or DOFO cells. A basic module of the flexible γ_t lattice is made of two to three FODO cells and a reflective symmetric doublet- or triplet-matching section. In this appendix, we examine the properties of the basic module with two FODO cells and a doublet matching cell configuration discussed in Sec. II B.

The basic module can be expressed as

$$M_a \left\{ \frac{1}{2} Q_F B Q_D B \frac{1}{2} Q_F \right\} M_b \left\{ Q_{F1} O_1 Q_{D2} O_2 \right\} M_c + \text{refl. sym. beam line} , \quad (\text{A1})$$

where $M_{a,b,c}$ are marker locations, Q 's are quadrupoles, O 's are drift spaces, and B 's stand for dipoles. The horizontal betatron transfer matrix of the FODO cell is given by

$$M_{\text{FODO}} = \begin{pmatrix} \cos \mu & \beta_F \sin \mu & D_F(1 - \cos \mu) \\ -\frac{1}{\beta_F} \sin \mu & \cos \mu & \frac{D_F}{\beta_F} \sin \mu \\ 0 & 0 & 1 \end{pmatrix} , \quad (\text{A2})$$

where μ is the horizontal phase advance in the FODO cell. We have assumed symmetry in the Courant-Snyder parameters at the center of the focusing quadrupole, i.e., $\beta'_F = 0$ and $D'_F = 0$.

In the thin-lens approximation with equal focusing and defocusing strengths, the Courant-Snyder parameters are given by

$$\sin \frac{\mu}{2} = \frac{L_F}{2f} , \quad \beta_F = \frac{2L_F(1 + \sin \frac{1}{2}\mu)}{\sin \mu} , \quad D_F = \frac{L_F\theta(2 + \sin \frac{1}{2}\mu)}{2 \sin^2 \frac{1}{2}\mu} , \quad (\text{A3})$$

where L_F is the length of the half FODO cell, f is the focal length of quadrupoles in the FODO cell, and θ is the bending angle of the dipole B . However it is worth pointing out that the applicability of Eq. (A2) is not limited to thin-lens approximation.

In the normal FODO lattice, the dispersion function is assumed to be periodic in each FODO cell. In this case, the dispersion function at the center of the focusing quadrupole is D_F with $D'_F = 0$. For an imaginary γ_t lattice, the dispersion function at the beginning of the FODO cell is prescribed with a value D_a with $D'_a = 0$ in order to achieve the preferable γ_t value. Depending on the initial dispersion value at marker M_a , the dispersion function at marker M_b is given by

$$D_b = D_F - (D_F - D_a) \cos \mu, \quad D'_b = \frac{D_F - D_a}{\beta_b} \sin \mu, \quad (\text{A4})$$

where β_b is the betatron amplitude function at marker M_b with $\beta_b = \beta_F$ of Eq. (A3). In the matching section (assuming that there is no dipole or negligible dipole contribution to dispersion), the dispersion action is invariant, i.e.,

$$2J_c = 2J_b = \frac{D_b^2}{\beta_b} + \beta_b D_b'^2 = 2J_F[1 - 2(1 - \zeta) \cos \mu + (1 - \zeta)^2], \quad (\text{A5})$$

with

$$\zeta = \frac{D_a}{D_F}. \quad (\text{A6})$$

Here, ζ is the ratio of the desired dispersion at marker M_a to that in the usually matched FODO cell lattice, and J_F is the dispersion action for the regular FODO cell at the focusing quadrupole location. Figure 26 shows J_b/J_F as a function of ζ for various phase advances per cell. Note here that the ratio of the dispersion actions increases when the initial dispersion D_a at marker M_a is chosen to be more negative. It is preferable to have a smaller dispersion action in the matching section in order to minimize the dispersion function of the module. One may like to conclude from Fig. 26 that a smaller phase advance in the FODO cell is preferred. However, it is worth pointing out that the dispersion action J_F for a 45° phase advance FODO cell is about 7.9 times larger than that for a 90° phase advance. Thus, the phase advance in the FODO cell should be 60° or larger in order to achieve a small dispersion action in the matching section.

The dispersion functions and other Courant-Snyder parameters are then matched at the symmetry point at marker M_c with a doublet (or triplet). The betatron transfer matrix is given by

$$M_{b \rightarrow c} = \begin{pmatrix} \sqrt{\frac{\beta_c}{\beta_b}} \cos \psi & \sqrt{\beta_b \beta_c} \sin \psi & 0 \\ -\frac{1}{\sqrt{\beta_b \beta_c}} \sin \psi & \sqrt{\frac{\beta_b}{\beta_c}} \cos \psi & 0 \\ 0 & 0 & 1 \end{pmatrix}, \quad (\text{A7})$$

where we have also assumed a symmetry condition at marker M_c for the Courant-Snyder parameters, i.e., $\beta'_b = 0$ and $\beta'_c = 0$. Here, β_b and β_c are the betatron amplitudes at, respectively, markers M_b and M_c , while ψ is the betatron phase advance between markers M_b and M_c .

The required dispersion matching condition at marker M_c is $D'_c = 0$. Using Eq. (A4), we obtain then

$$\tan \psi = \frac{(1-\zeta) \sin \mu}{1 - (1-\zeta) \cos \mu} . \quad (\text{A8})$$

This means that the phase advance of the matching section is not a free parameter, but is determined completely by the initial dispersion value D_a at marker M_a and the phase advance of the FODO cell. This condition is independent of whether we use a doublet or a triplet for the betatron-parameter matching. In the example discussed in Sec. II, it is preferable to use a doublet matching section. Figure 27 shows the required phase advance in the matching section as a function of phase advance μ of the FODO cell for various values of $\zeta = D_a/D_F$. The total phase advance of the whole basic module is then given by $2(\mu + \psi)$, which is a function of only the desired dispersion function at marker M_a and the phase advance μ in the FODO cell. Figure 28 shows the total phase advance of the whole module as a function of the phase advance of the FODO cell for $\zeta = -0.3$ to -0.6 .

Quadrupoles Q_{F1} and Q_{D2} in the matching section are then adjusted to achieve the required phase advance ψ given by Eq. (A8). A low betatron amplitude function at marker M_c is desired so that D_C will be small. Care should also be taken in the arrangement and choices of quadrupoles Q_{F1} and Q_{D2} in order to achieve reasonably small vertical Courant-Snyder parameters. Then, the matching becomes relatively simple as was demonstrated in Sec. II B.

From the beam dynamics point of view, a basic module with a phase advance of $\frac{3}{2}\pi$ is preferable due to the cancellation in the systematic half-integer stopband and the sextupole distortion functions. To achieve a $\frac{3}{2}\pi$ phase advance, $\zeta \approx -0.3 \sim -0.4$ and a phase advance per FODO cell of $\mu = 60^\circ$ to 75° can be used. With a less negative ζ value, however, the γ_t value will have larger imaginary value. Careful design and compromise can be achieved as was shown in Sec. III.

The dispersion values at the midpoints of dipoles in the FODO cell are given by

$$D_{B1} = D_a(1 - \frac{1}{2} \sin \frac{1}{2}\mu) , \quad D_{B2} = D_a(1 - \frac{1}{2} \sin \frac{1}{2}\mu) + (D_F - D_a) \sin^2 \frac{1}{2}\mu . \quad (\text{A9})$$

In the thin-element approximation, the momentum compaction becomes

$$\alpha = \frac{1}{L_m} \sum_{\text{modules}} (D_{B1} + D_{B2})\theta , \quad (\text{A10})$$

where θ is the bending angle of each dipole and L_m is the length of the half-module. In comparison with the momentum compaction factor of a lattice made from conventional FODO cells, we obtain

$$\frac{\alpha}{\alpha_{\text{FODO}}} = \frac{L_F}{L_m} \left[\zeta + (1-\zeta) \frac{\sin^2 \frac{1}{2}\mu}{2(1 - \frac{1}{2}\sin \frac{1}{2}\mu)} \right]. \quad (\text{A11})$$

Note here that the momentum compaction factor is a linear function of the initial dispersion function if the module length is a constant. Although the thin-lens approximation has been used for the quadrupoles and dipoles, it is easy to see that this linear relationship is exact even for thick elements. If the horizontal phase advance μ_x of the FODO cell is different from its vertical phase advance μ_y , Eqs. (A9) and (A10) still hold when the replacements,

$$\begin{aligned} \sin^2 \frac{1}{2}\mu &\rightarrow \sin^2 \frac{1}{2}\mu_x, \\ \frac{1}{2} \sin \frac{1}{2}\mu &\rightarrow \frac{1}{8} \left(s_- + \sqrt{s_-^2 + 8s_+} \right), \end{aligned} \quad (\text{A12})$$

are made, where $s_{\pm} = \sin^2 \frac{1}{2}\mu_x \pm \sin^2 \frac{1}{2}\mu_y$. This linear relationship was demonstrated in Fig. 3 using the examples of Table I and Fig. 2. For those cases, the horizontal and vertical phase advances for the FODO cells are, respectively, 65.16° and 106.20° . The momentum compaction factor of the module becomes zero or the module isochronous at $\zeta = -0.261$. However, this occurs actually at $\zeta = -0.35$ instead according to Fig. 3. The discrepancy is due to the positive contribution of the extra dipole in the low-beta matching section of the module.

The above analysis can be applied also to a DOFO cell discussed in our previous study [7]. In the case with DOFO cells, the variables with the subscript F in Eqs. (A1) to (A4) should be replaced with the values at the defocusing quadrupole. In fact, J_D is slightly larger than J_F . A slightly larger ζ has to be used in order to minimize the magnitude of the dispersion function in the module, because the dispersion value at the defocusing quadrupole location is smaller than that at the focusing quadrupole location. From Fig. 27, we observe therefore that a larger phase advance should be used in the matching section, where a triplet should be used. It becomes harder, however, to achieve the condition of $\frac{3}{2}\pi$ phase advance in the basic module.

For some economical reason, one may try to use DOFODO in place of the FODO cell in Eq. (A1), i.e., three FODO cells instead of two are placed inside a basic module. The betatron transfer matrix in the DOFODO cell becomes

$$M_{a \rightarrow b} = \begin{pmatrix} \sqrt{\frac{\beta_F}{\beta_D}} \cos \frac{3}{2}\mu & \sqrt{\beta_F \beta_D} \sin \frac{3}{2}\mu & D_F - D_D \sqrt{\frac{\beta_F}{\beta_D}} \cos \frac{3}{2}\mu \\ -\frac{1}{\sqrt{\beta_F \beta_D}} \sin \frac{3}{2}\mu & \sqrt{\frac{\beta_D}{\beta_F}} \cos \frac{3}{2}\mu & \frac{D_D}{\sqrt{\beta_F \beta_D}} \sin \frac{3}{2}\mu \\ 0 & 0 & 1 \end{pmatrix}, \quad (\text{A13})$$

where μ is the phase advance of a FODO cell, β_F , β_D , D_F , D_D are, respectively, betatron amplitudes and dispersion values at the focusing and defocusing quadrupoles of the FODO cell. Similar analysis as shown in this appendix can be repeated easily. The result will be a larger total dispersion value with less favorable phase advance for the module.

REFERENCES

- [1] E.D. Courant and H.S. Snyder, *Theory of the Alternating Gradient Synchrotron*, Ann. Phys. **3**, 1 (1958).
- [2] S.Y. Lee and J.M. Wang, *Microwave Instabilities across the Transition Energies*, IEEE Trans. Nucl. Sci. **NS-32**, 2323 (1985).
- [3] R. Gupta and J.I.M. Botman, *High Transition Energy Magnet Lattices*, IEEE Trans. Nucl. Sci. **NS-32**, 2308 (1985).
- [4] T. Collins, *Beta Theory*, Technical Memo, Fermilab, 1988
- [5] G. Guignard, *A Lattice with no Transition and Largest Aperture*, Proc. of 1989 IEEE Part. Accel. Conf., March 20-23, 1989, Chicago, IL, pp 915-917.
- [6] D. Trbojevic, D. Finley, R. Gerig, and S. Holmes, *Design Method for High Energy Accelerator without Transition Energy*, Proc. of Second European Particle Accelerator Conference, Nice, France, June 1990, pp 1536-1538.
- [7] K.Y. Ng, D. Trbojevic, and S.Y. Lee, *A Transitionless Lattice for the Fermilab Main Injector*, Proc. of 1991 IEEE Part. Accel. Conf., May 6-9, 1991, San Francisco, California, pp 159-161.
- [8] E.D. Courant, A.A. Garren, and U. Wienands, *Low Momentum Compaction Lattice Study for the SSC Low Energy Booster*, Proc. of 1991 IEEE Part. Accel. Conf., May 6-9, 1991, San Francisco, California, pp 2829-2831.
- [9] D. Johnson, *120 GeV Beam Line Design*, Fermilab Internal Report MI-0007, pp. 1-4, 1992.
- [10] F. Willeke, *Chromaticity Correction with Sextupoles*, US Accelerator School, unwritten.
- [11] B. Autin, *Nonlinear Betatron Oscillations*, CERN Report, pp. 1-25.
- [12] S.Y. Lee et al., *The Chromatic Correction in RHIC*, Proc. of 1987 IEEE Part. Accel. Conf., p. 1328, (1987).
- [13] K.Y. Ng, *Distortion Functions*, KEK Report 87-11, September 1987, pp. 1-17.

- [14] K.Y. Ng, *Comparison of the Second Order Tune Shift Formulas due to Sextupoles given by Collins and Ohnuma*, Fermilab Internal Report TM-1277, 1984.
- [15] B. Autin and F. Willeke, *Second Order Tune Shift in a Compensated Super Cell*, Second Advanced ICFA Beam Dynamics Workshop, Lugano, Switzerland, 11-16 April 1988, pp. 192-196.
- [16] H. Bruck, *Théory et Technique des Accélérateurs de Particules*, Saclay Institut National des Science et Technique Nucléaires, 1957.
- [17] L. Schachinger and R. Talman, *TEAPOT — A Thin Element Accelerator Program for Optics and Tracking*, SSC Central Design Group internal report SSC-52, 1985.
- [18] G.V.V. Vladimirski and E.K. Tarasov, *Theoretical Problems of the Ring Accelerators*, USSR Academy of Sciences, Moskow, 1955.

TABLES

TABLE I. Variation of γ_t as a function of D_{\min} showing modules with FODO Cells of fixed tunes: $\nu_x = 0.181$, $\nu_y = 0.295$.

γ_t	ν_x	ν_y	D_{\max} [m]	D_{\min} [m]
<i>i</i> 23.275	0.83579	0.93727	0.81343	-2.50000
<i>i</i> 26.935	0.81710	0.85538	0.77439	-2.00000
<i>i</i> 35.039	0.79452	0.76733	0.77516	-1.50000
<i>i</i> 80.440	0.76767	0.80456	0.98849	-1.00000
<i>i</i> 461.607	0.76033	0.81404	1.03838	-0.88000
<i>i</i> 671.104	0.76021	0.81421	1.03923	-0.87800
<i>i</i> 789.966	0.76018	0.81425	1.03944	-0.87750
<i>i</i> 1007.845	0.76014	0.81429	1.03965	-0.87700
816.158	0.76002	0.87500	1.04071	-0.87500
502.835	0.75989	0.87300	1.04131	-0.87300
268.897	0.75939	0.81531	1.04472	-0.86500
120.311	0.75652	0.81882	1.06317	-0.82000
80.518	0.75196	0.82604	1.09472	-0.75000
47.123	0.73448	0.84777	1.19941	-0.50000
36.859	0.71503	0.87015	1.29385	-0.25000
25.266	0.64343	0.92643	1.62542	0.42900
21.574	0.58485	0.93472	1.83655	0.66500
18.841	0.52070	0.90784	2.04859	0.87400
15.885	0.42758	0.89983	2.67670	1.17600

TABLE II. Modules with FODO Cells of $\nu_x = 0.142$, $\nu_y = 0.135$.

γ_t	ν_x	ν_y	D_{\max} [m]	D_{\min} [m]
<i>i</i> 57.309	0.71696	0.33830	0.81914	-0.81500

TABLE III. Modules with FODO Cells of $\nu_x = 0.147$, $\nu_y = 0.2155$.

γ_t	ν_x	ν_y	D_{\max} [m]	D_{\min} [m]
$i67.121$	0.71993	0.38893	0.77117	-0.79000

TABLE IV. Courant-Snyder parameters of a module with just 3 FODO cells in a row.

γ_t	ν_x	ν_y	β_x [m]	D_{\max} [m]	D_{\min} [m]	ν_x/cell	ν_y/cell
13.754	0.54310	0.88502	52.825	2.52916	1.28890	0.181	0.295
18.734	0.75000	0.75600	45.949	1.42843	0.69000	0.250	0.252

TABLE V. Off-momentum Properties of the imaginary γ_t lattice.

	1.5%	-1.5%
$\Delta\sqrt{\beta_x}/\sqrt{\beta_x}$ [%]	8.23	5.96
$\Delta\sqrt{\beta_y}/\sqrt{\beta_y}$ [%]	11.94	7.01
$\Delta D/D$ ($D > 0$) [%]	-6.57	11.20
$\Delta D/D$ ($D < 0$) [%]	17.20	22.40
$x_{\text{co,max}}$ [mm]	45.40	42.50
$x_{\text{co,min}}$ [mm]	-46.80	-43.30
γ_t	$i26.44$	$i33.91$
$\Delta\nu_x$	0.0081	0.0577
$\Delta\nu_y$	0.0476	0.0450

TABLE VI. Comparison of dispersion of FODO Lattices with imaginary γ_t lattices.

γ_t	ν_x	ν_y	D_{\max} [m]	D_{\min} [m]
11.54	0.250	0.252	3.800	1.825
$i28.65$	0.161	0.157	2.060	-2.700
21.59	0.250	0.252	1.978	1.171
$i56.7$	0.165	0.180	1.180	-1.259

TABLE VII. Phases advances for the three modules.

	$\Delta\psi_x/2\pi$	$2\Delta\psi_y/2\pi$
BASIC	0.7524	0.7603
EXTR1	0.7391	0.7163
EXTR2	0.7450	0.7334

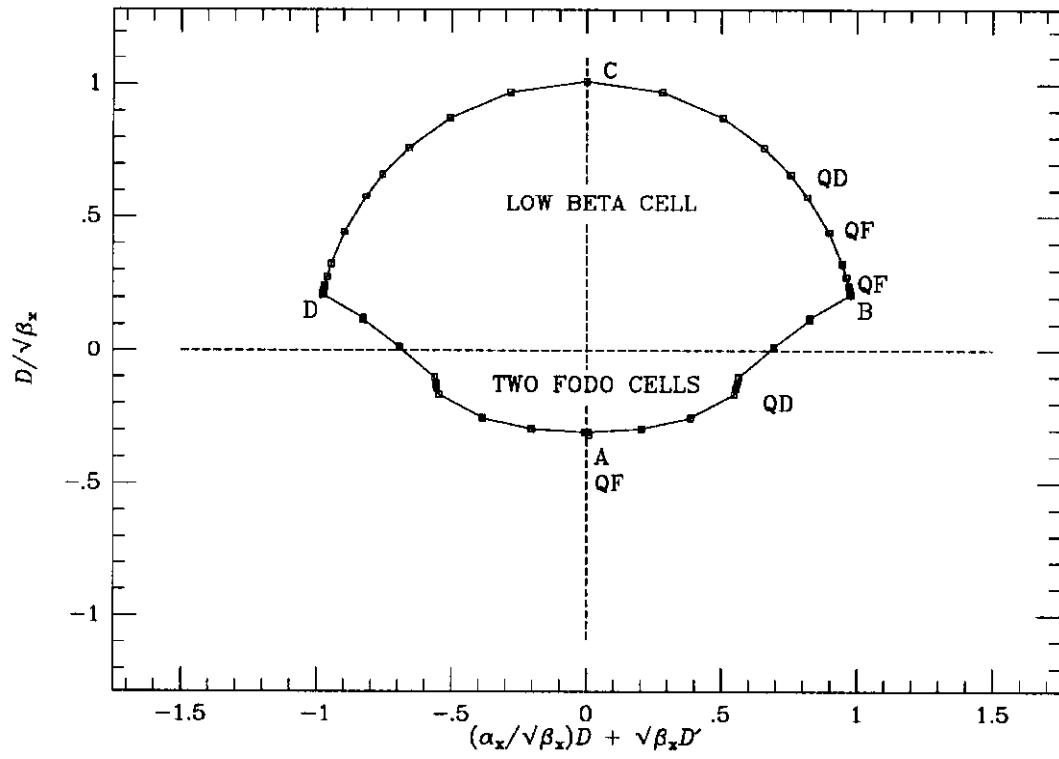


Figure 1

FIG. 1. Normalized horizontal dispersion function in the basic module of the imaginary γ_t lattice.

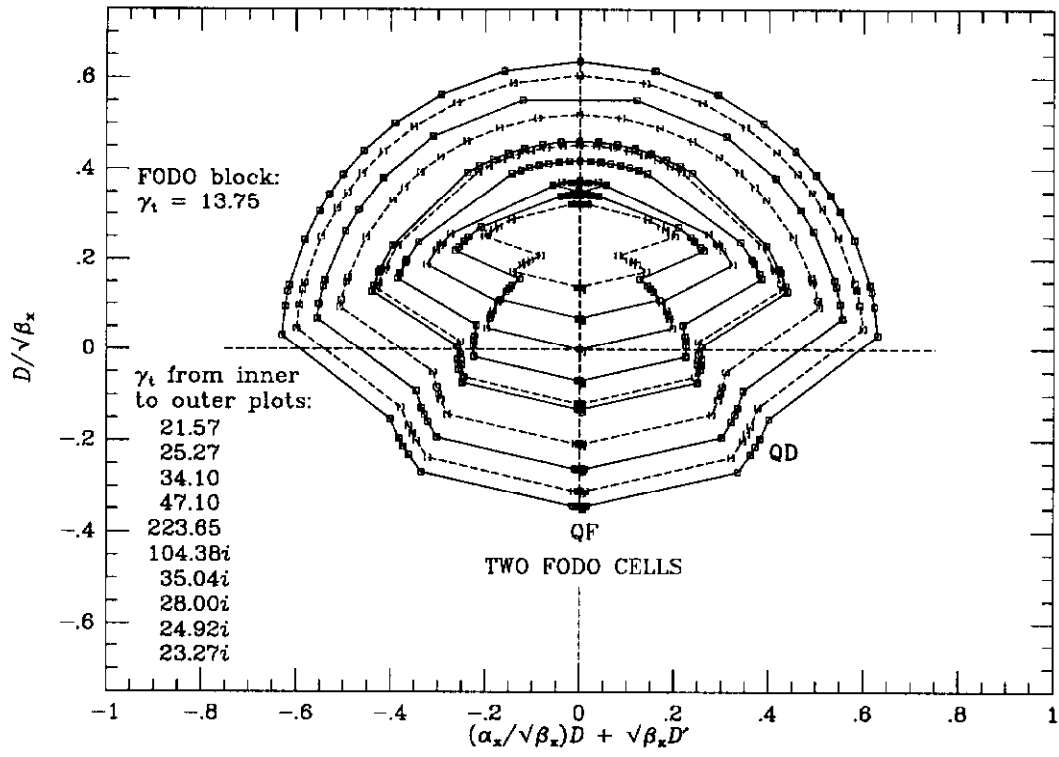


Figure 2

FIG. 2. Dependence of the γ_t values on the χ_{\min} of the basic imaginary- γ_t module with the same FODO cells presented in the normalized horizontal dispersion-function space.

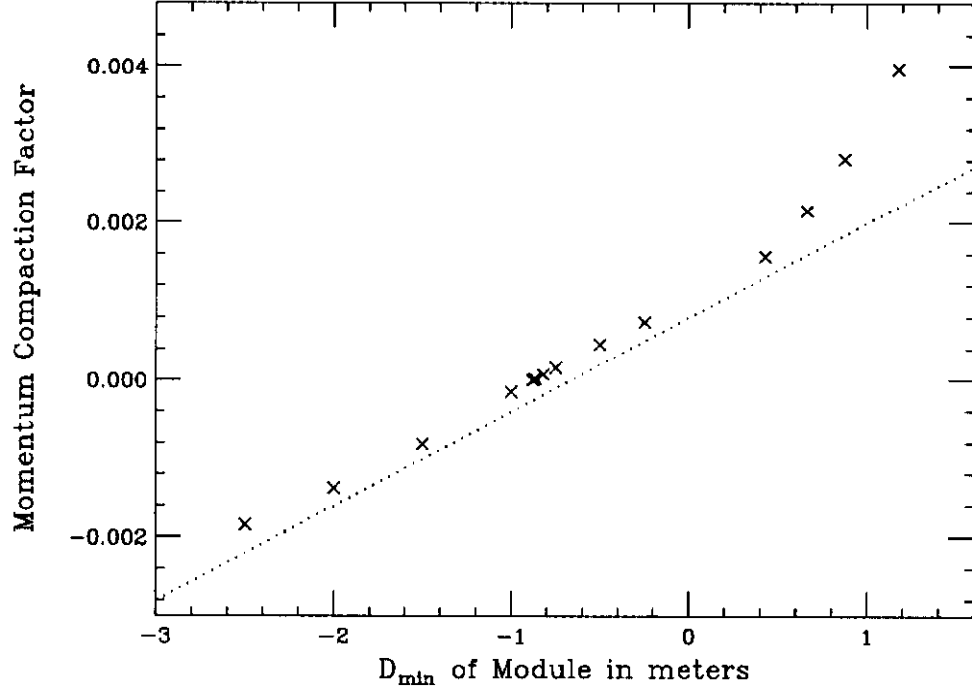


Figure 3

FIG. 3. Plot of momentum compaction factor as a function of minimum dispersion for the modules discussed in Table I and Fig. 2. The dotted line is the linear relationship predicted analytically by Eq. (A10) in the appendix with the dipole in the low-beta matching section omitted.

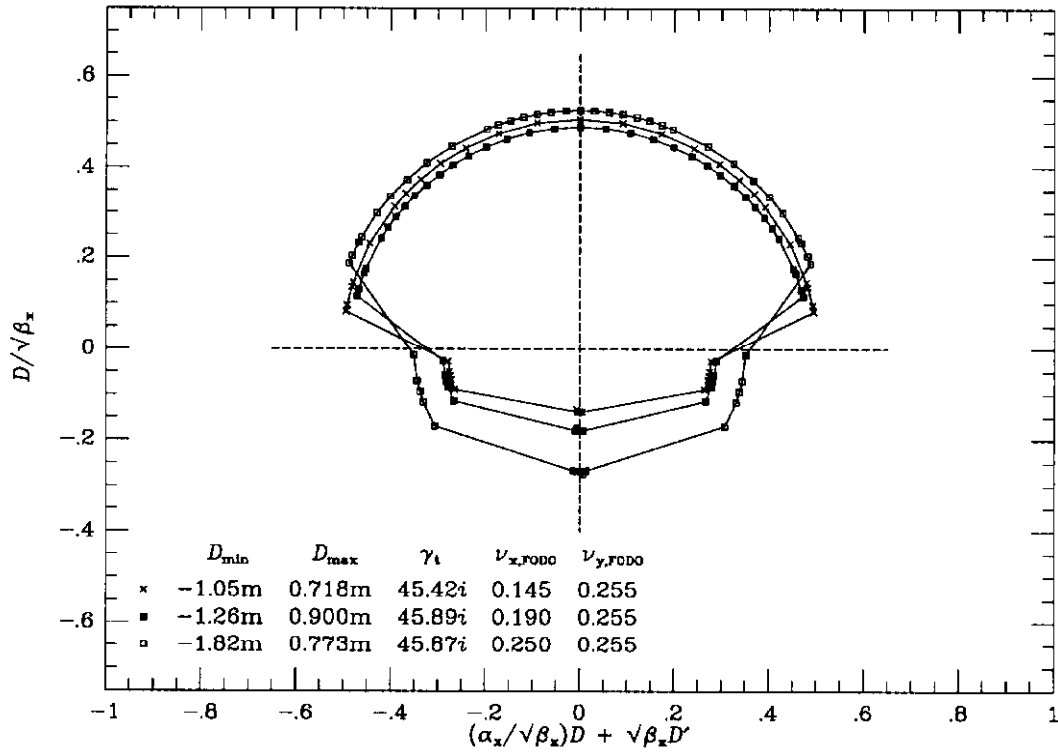


Figure 4

FIG. 4. Normalized dispersion ξ - χ plots for modules with FODO cells of different phase advances.

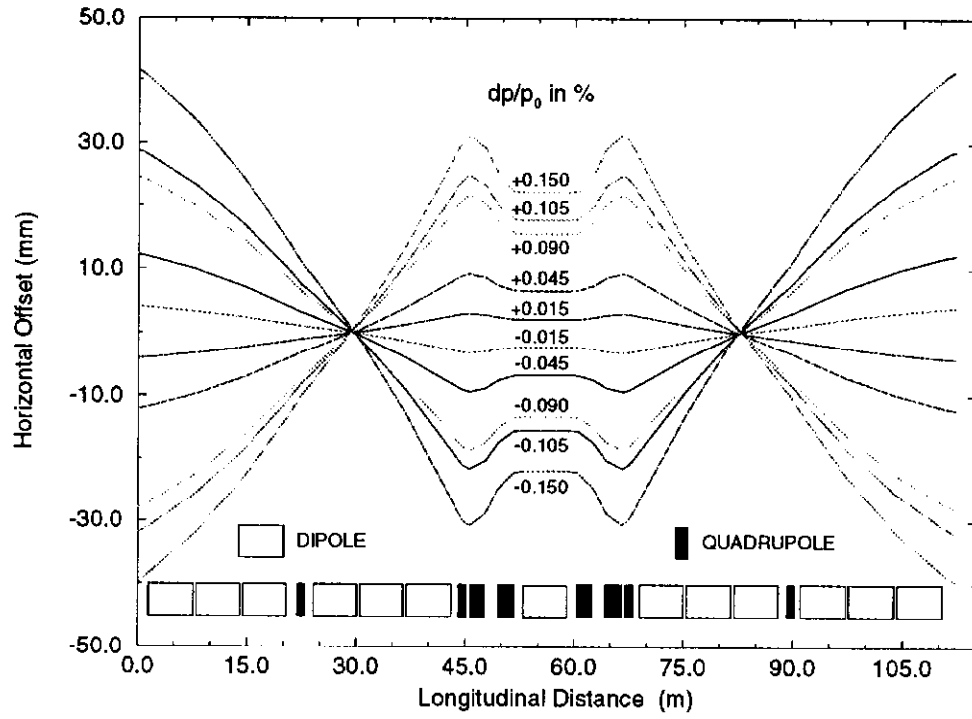


Figure 5

FIG. 5. Horizontal closed orbits of off-momentum particles in the basic block of the imaginary γ_t lattice.

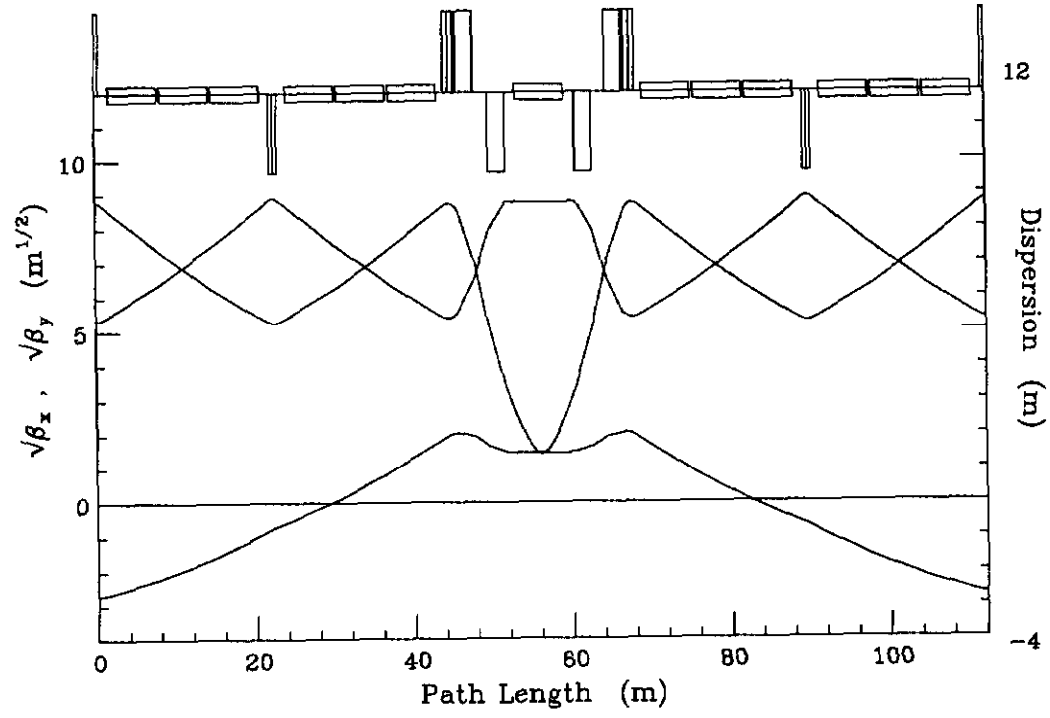


Figure 6

FIG. 6. Betatron functions and dispersion function within the basic module of the imaginary γ_t lattice.

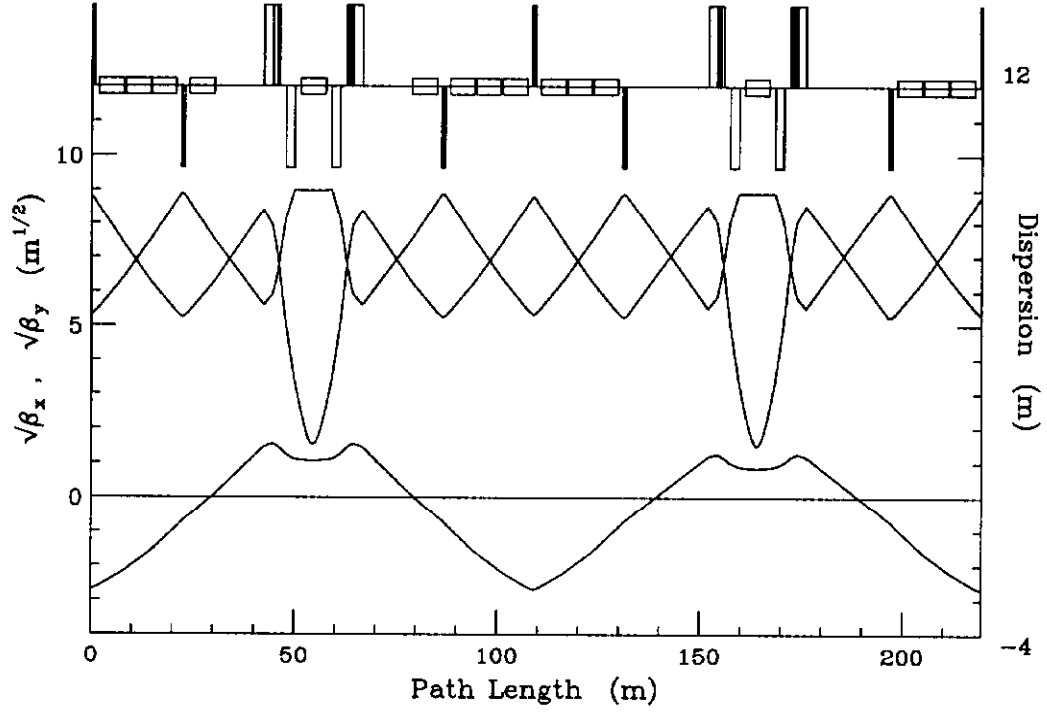


Figure 7

FIG. 7. Betatron functions and dispersion function within the injection and extraction module of the imaginary γ_t lattice.

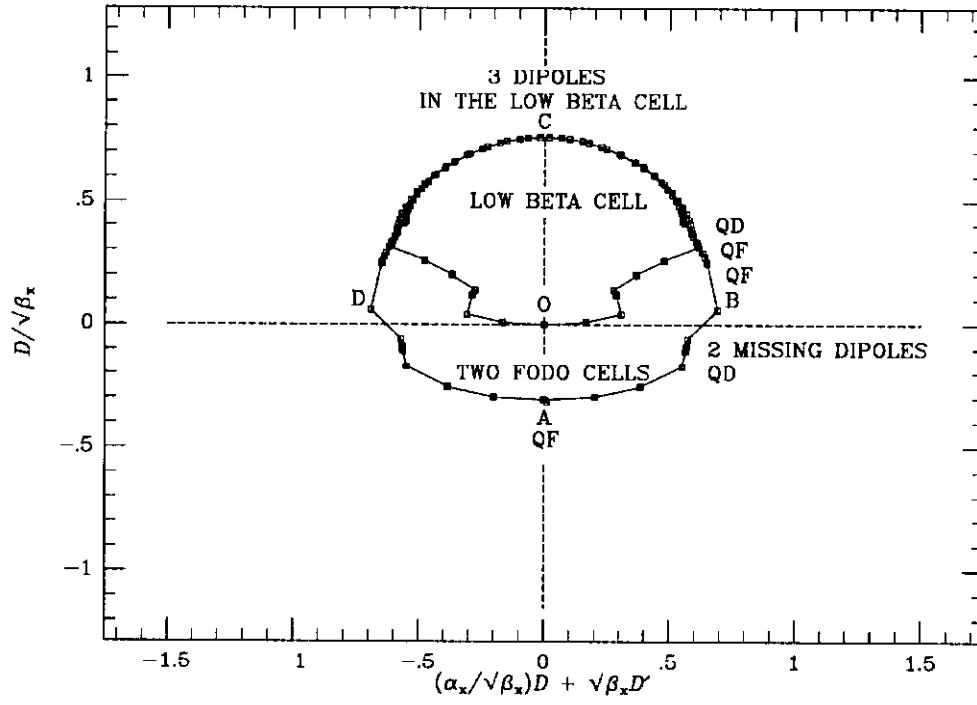


Figure 8

FIG. 8. Normalized dispersion ξ - χ plot for the zero-dispersion straight section.

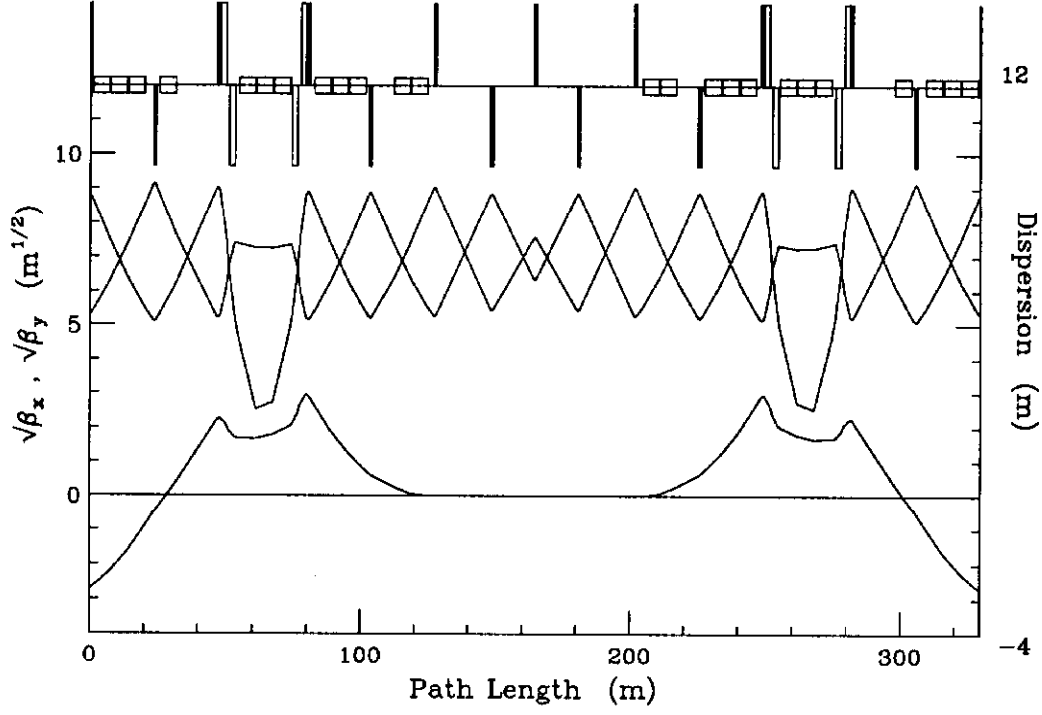


Figure 9

FIG. 9. Betatron functions and dispersion function within the module with dispersion-free straight section of the imaginary γ_t lattice.

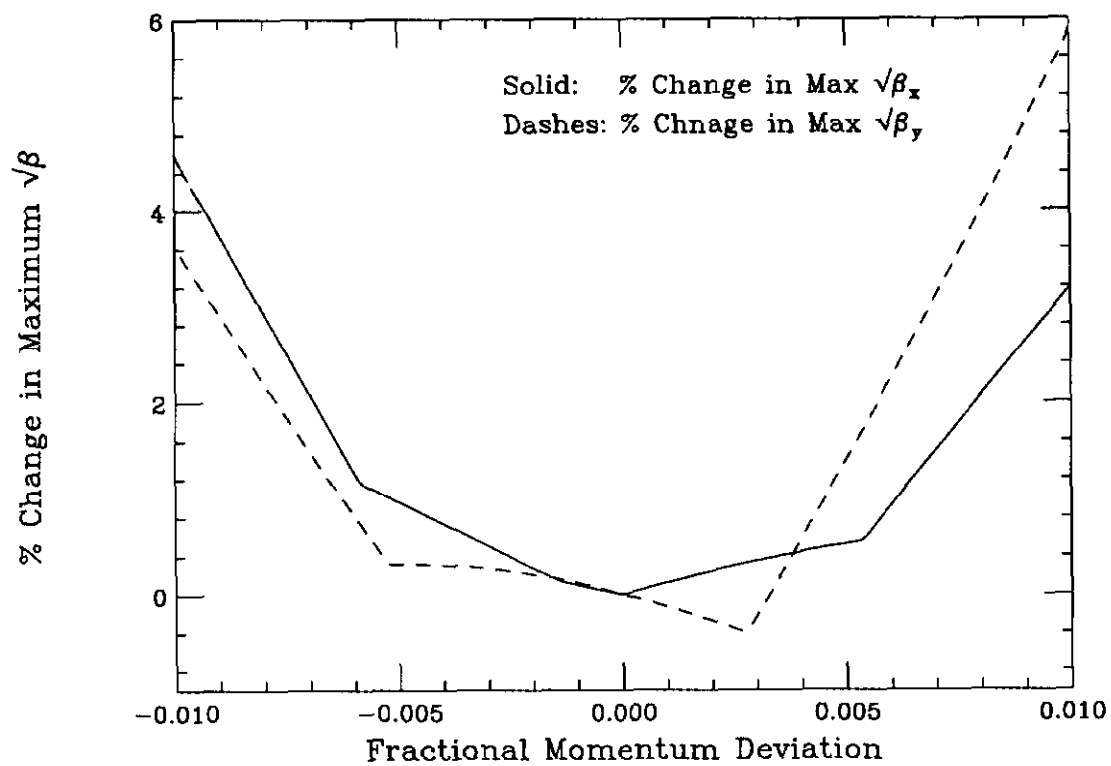


Figure 10

FIG. 10. Dependences of maximum betatron functions on momentum.

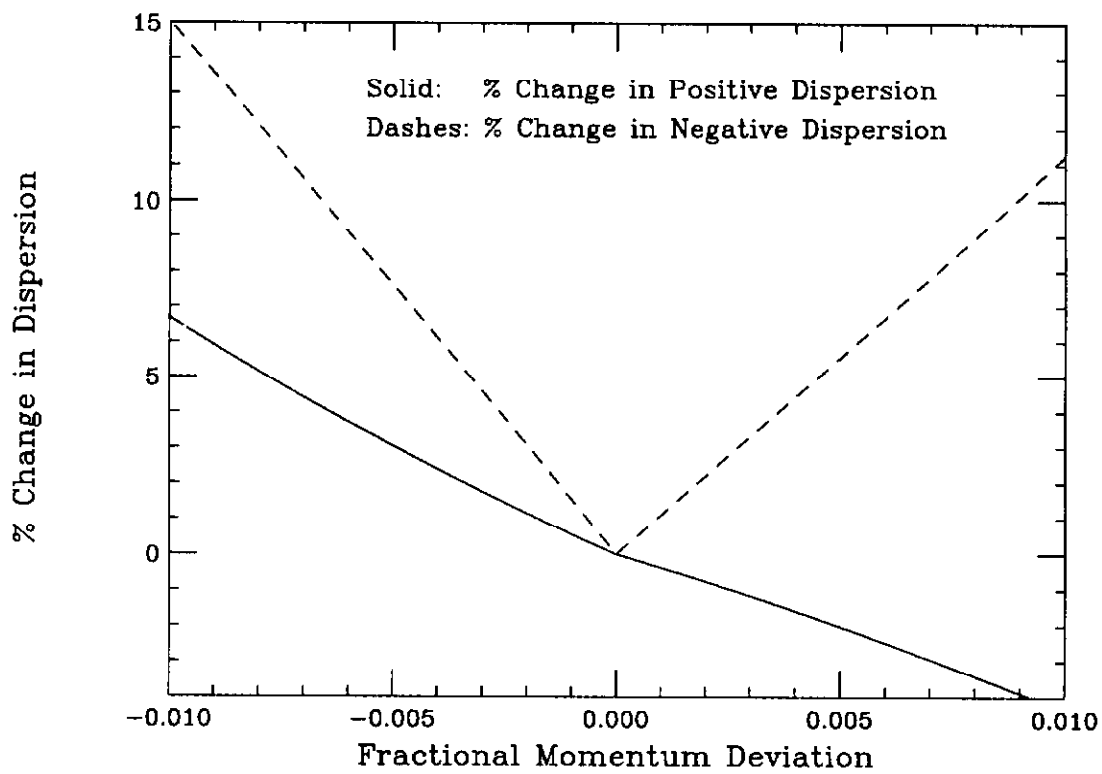


Figure 11

FIG. 11. Dependence of the maximum horizontal dispersion change on momentum.

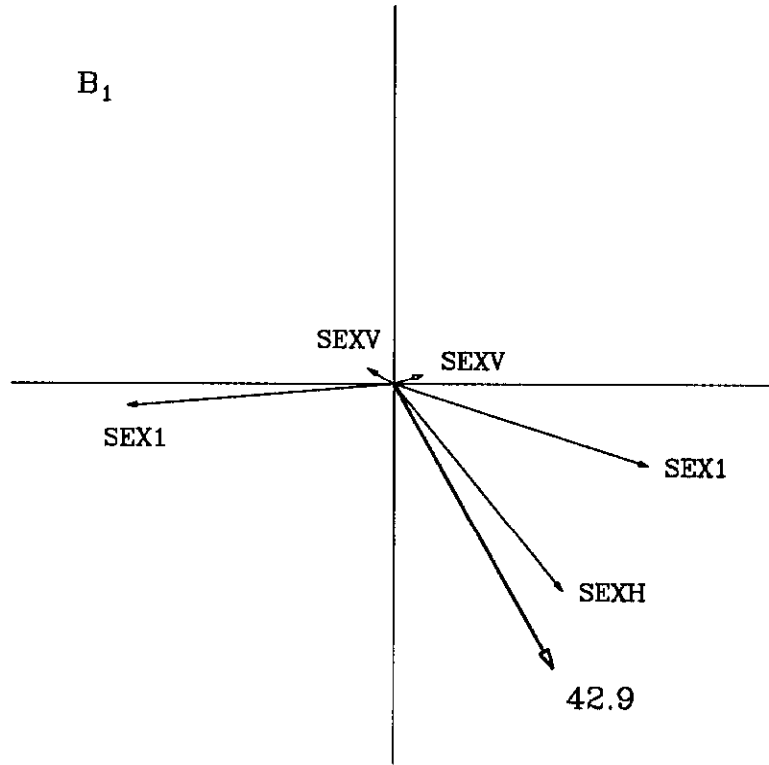


Figure 12

FIG. 12. Contribution to B_1 of the 5 sextupoles in the first BASIC module in the 12-module row. The sum is represented by the darker arrow with its magnitude.

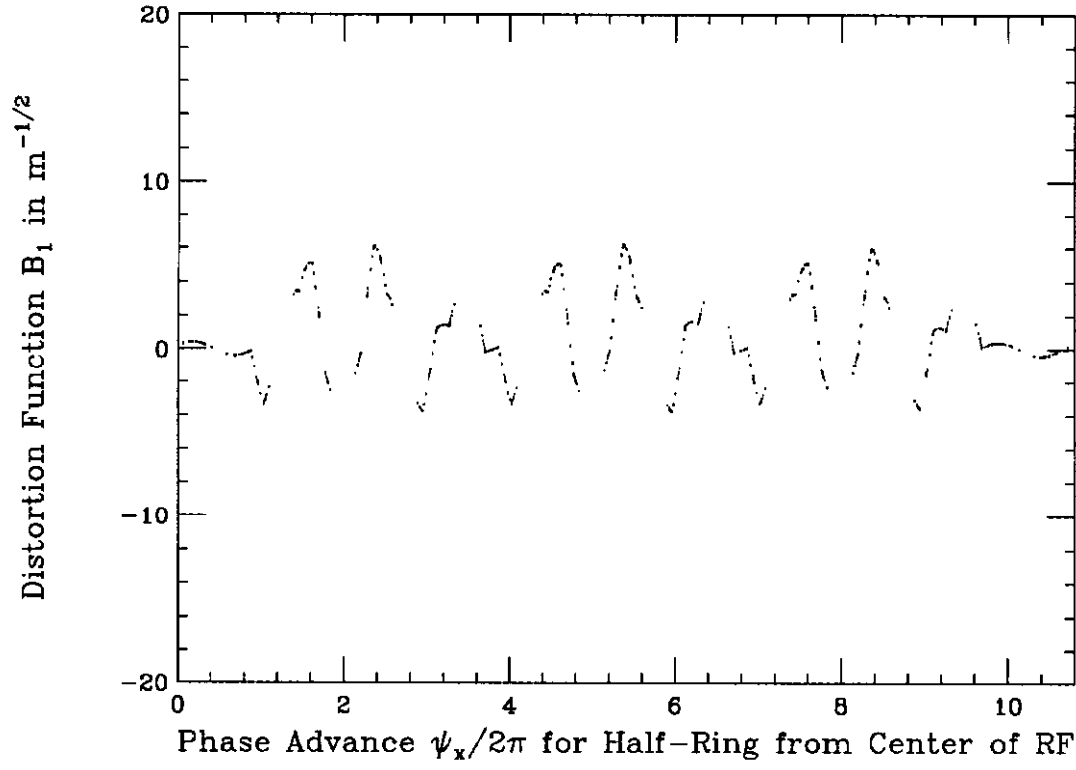


Figure 13

FIG. 13. Plot of distortion function B_1 as a function of phase advance $\psi_x/2\pi$ for half the ring starting from the center of an rf straight.

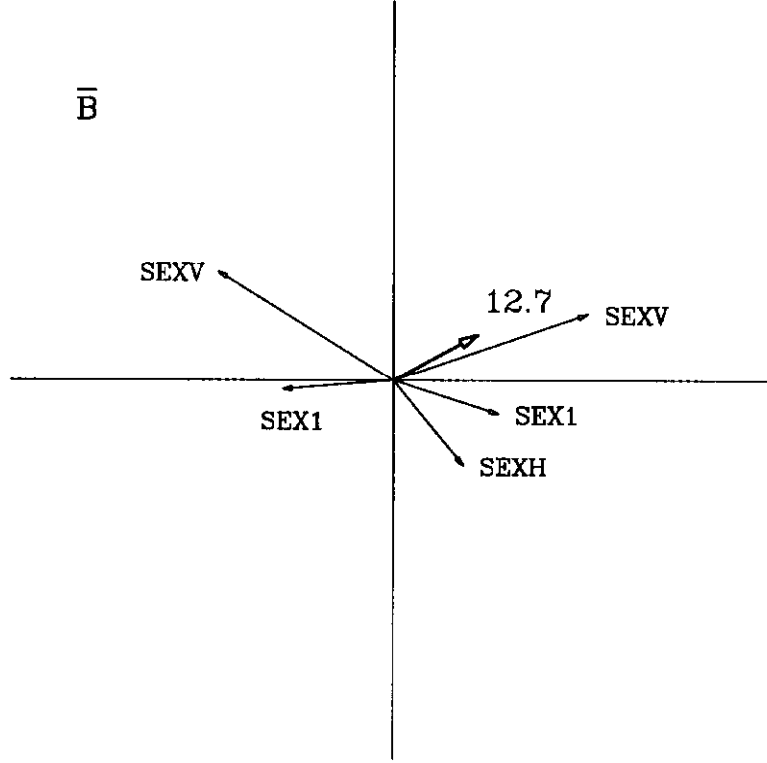


Figure 14

FIG. 14. Contribution to $\bar{\mathbf{B}}$ of the 5 sextupoles in the first BASIC module in the 12-module row. The sum is represented by the darker arrow with its magnitude.

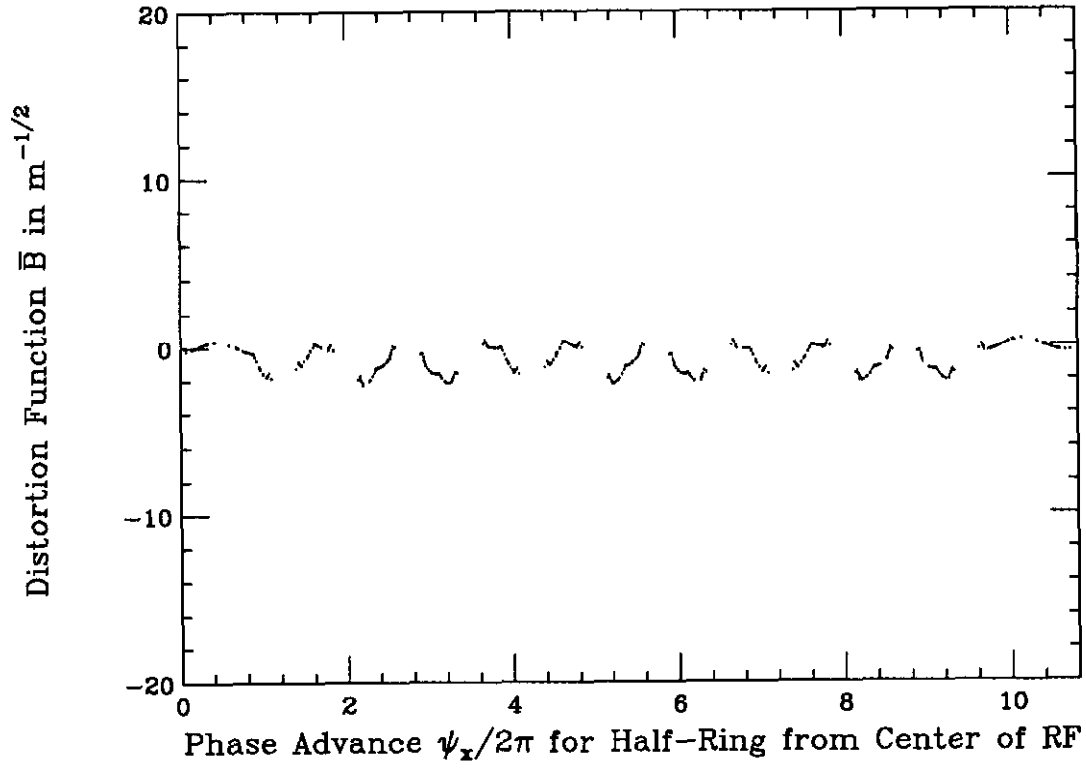


Figure 15

FIG. 15. Plot of distortion function \bar{B} as a function of phase advance $\psi_x/2\pi$ for half the ring starting from the center of an rf straight.

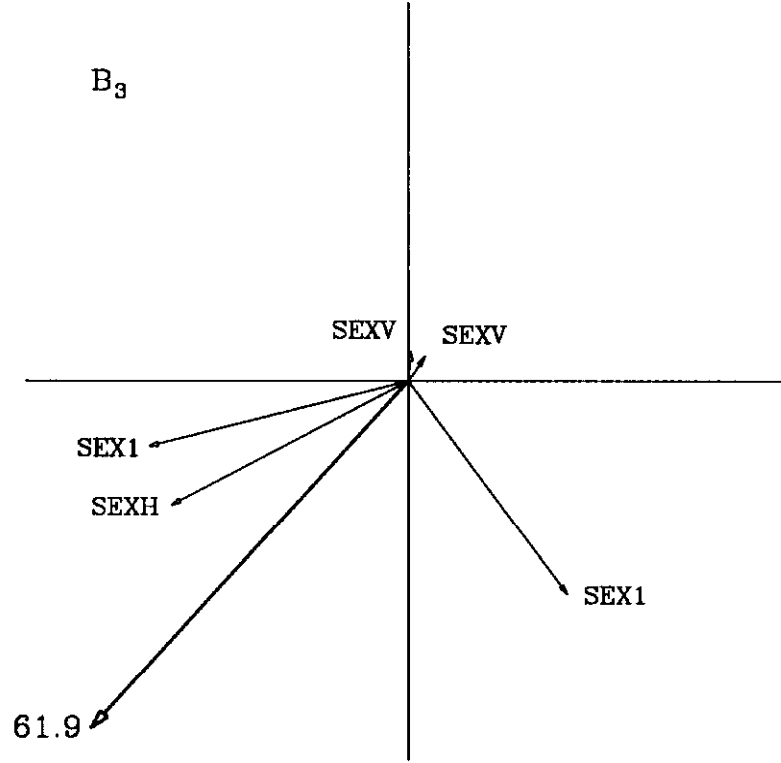


Figure 16

FIG. 16. Contribution to \mathbf{B}_3 of the 5 sextupoles in the first BASIC module in the 12-module row. The sum is represented by the darker arrow with its magnitude.

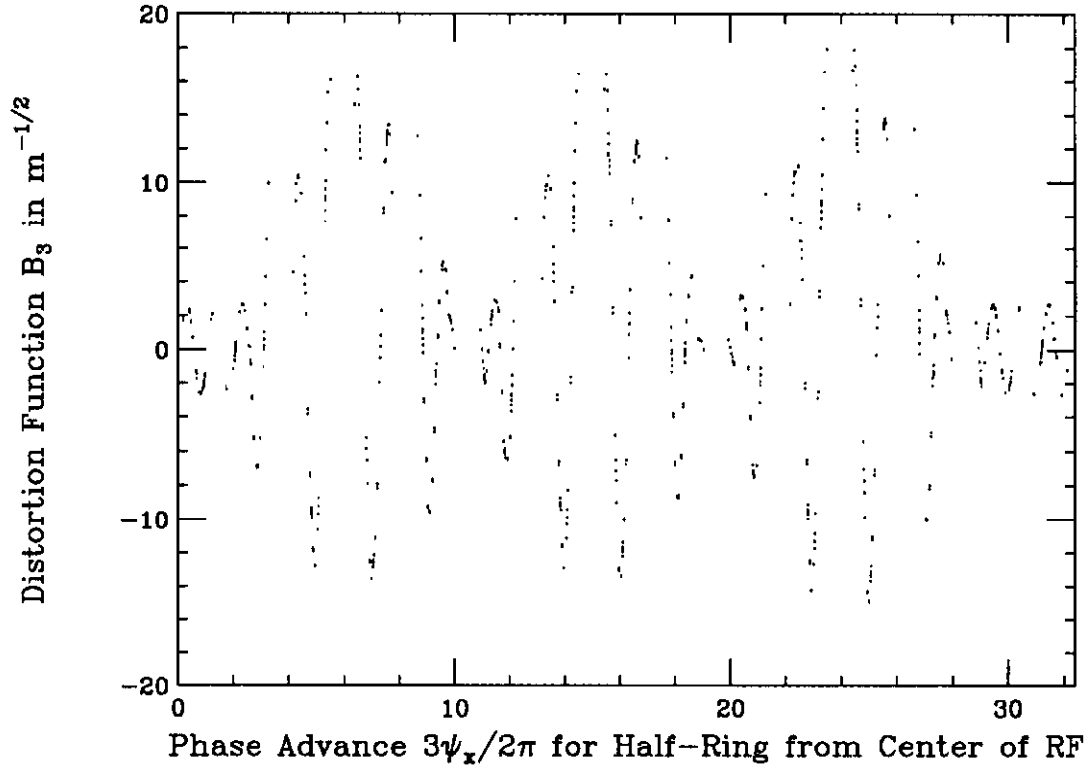


Figure 17

FIG. 17. Plot of distortion function B_3 as a function of phase advance $\psi_x/2\pi$ for half the ring starting from the center of an rf straight.

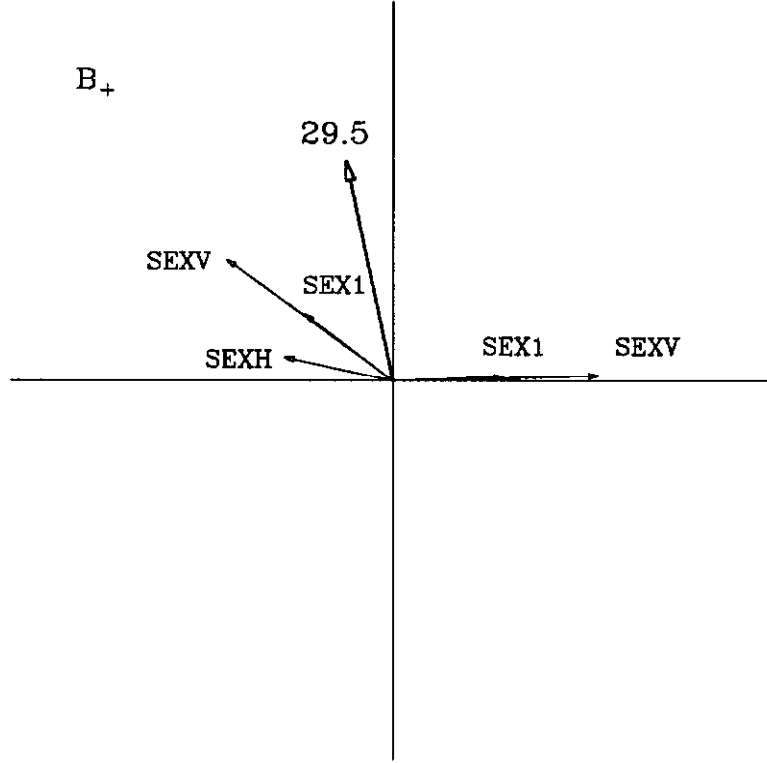


Figure 18

FIG. 18. Contribution to \mathbf{B}_+ of the 5 sextupoles in the first BASIC module in the 12-module row. The sum is represented by the darker arrow with its magnitude.

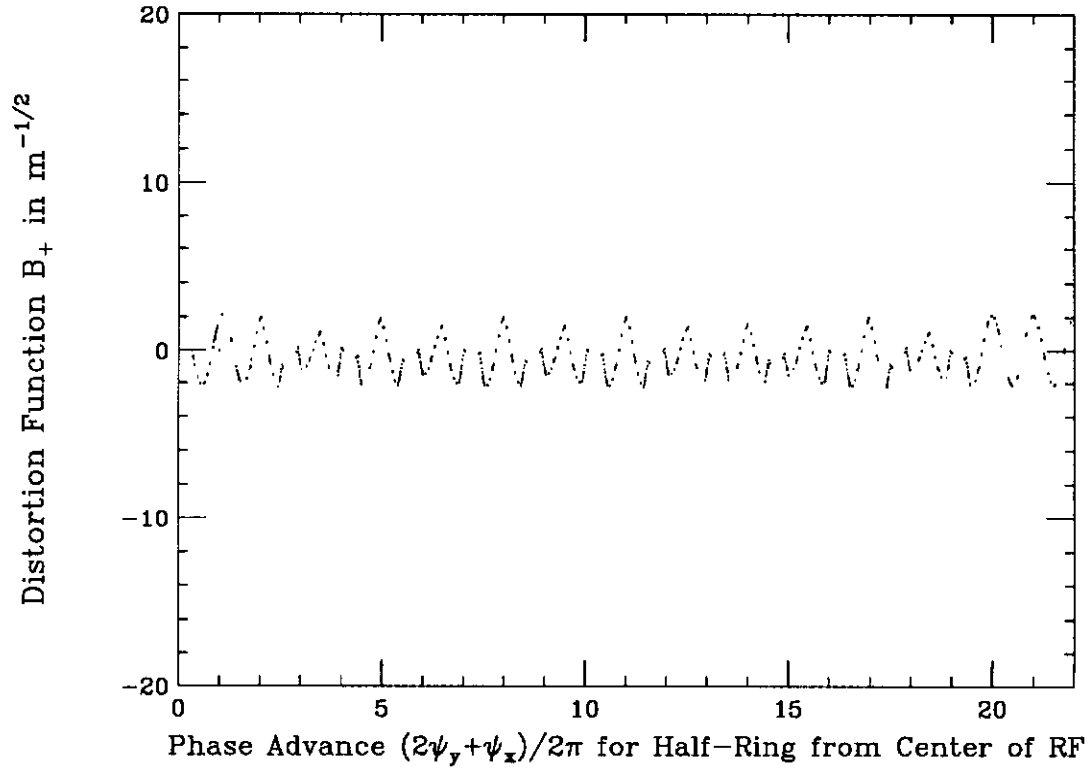


Figure 19

FIG. 19. Plot of distortion function B_+ as a function of phase advance $\psi_+/2\pi = (2\psi_y + \psi_x)/2\pi$ for half the ring starting from the center of an rf straight.

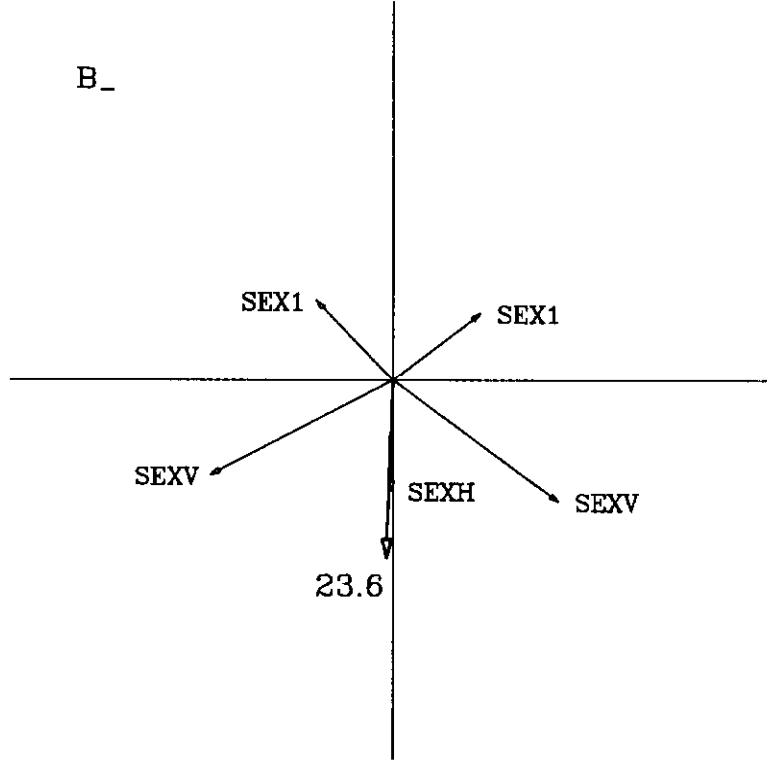


Figure 20

FIG. 20. Contribution to \mathbf{B}_- of the 5 sextupoles in the first BASIC module in the 12-module row. The sum is represented by the darker arrow with its magnitude.

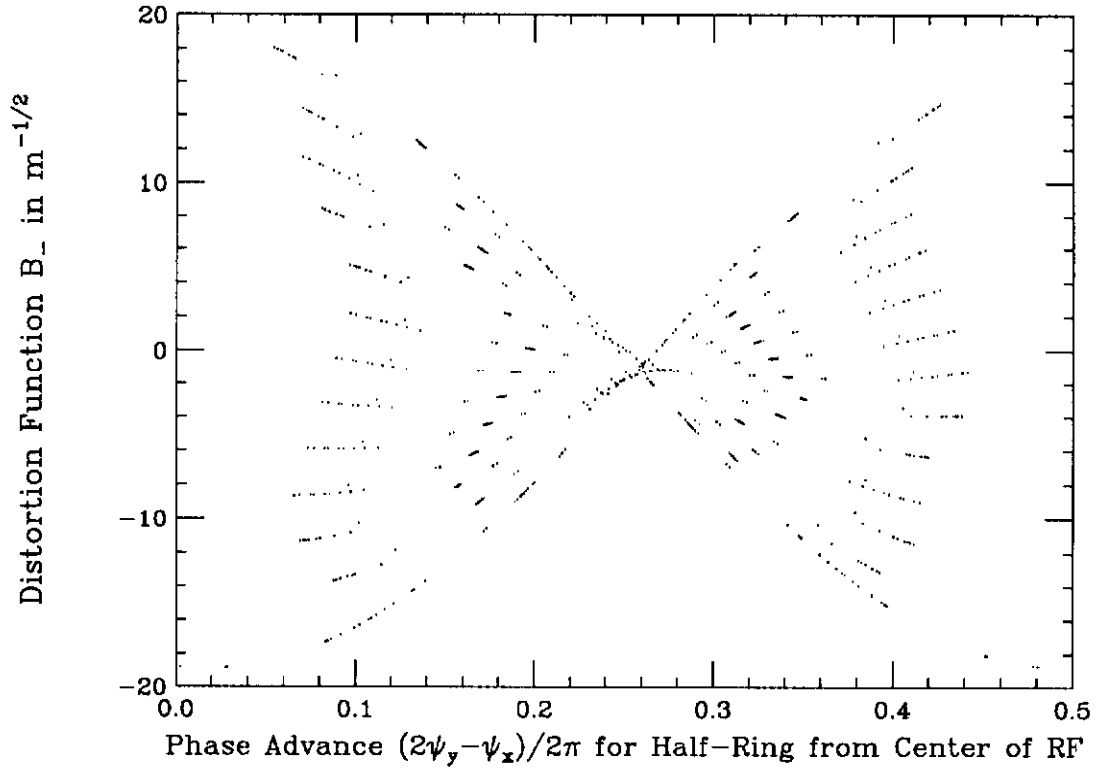


Figure 21

FIG. 21. Plot of distortion function B_+ as a function of phase advance $\psi_-/2\pi = (2\psi_y - \psi_-)/2\pi$ for half the ring starting from the center of an rf straight.

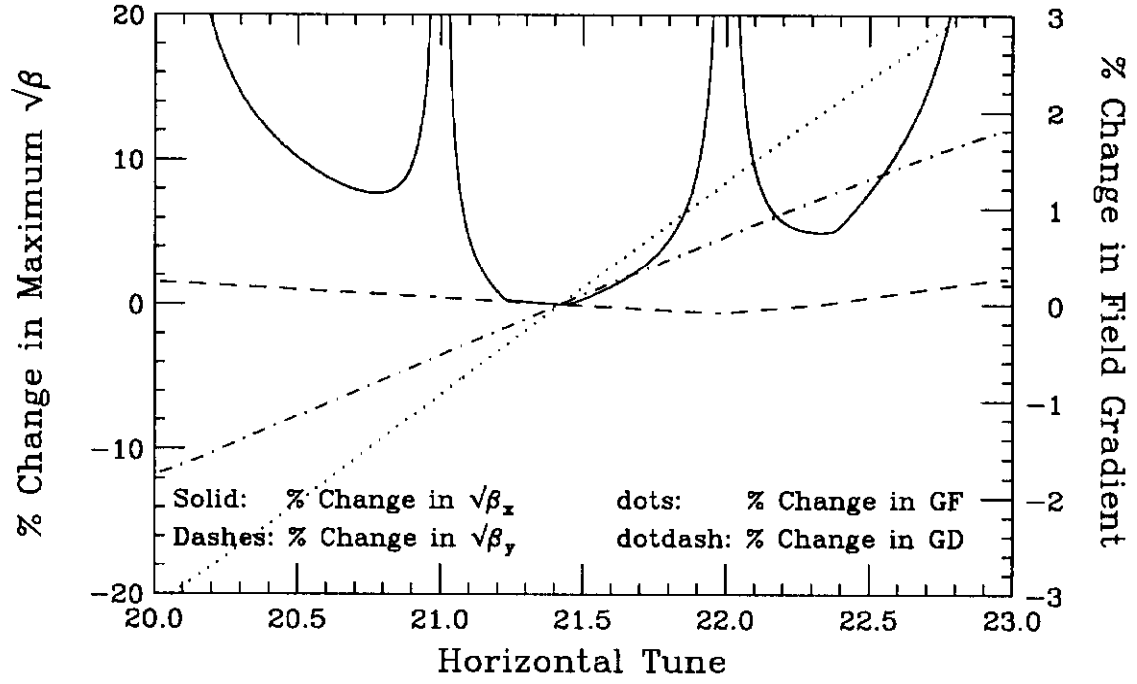


Figure 22

FIG. 22. Betatron-function ($\sqrt{\beta_x}$ and $\sqrt{\beta_y}$) dependences on the horizontal tune, the vertical tune being kept constant.

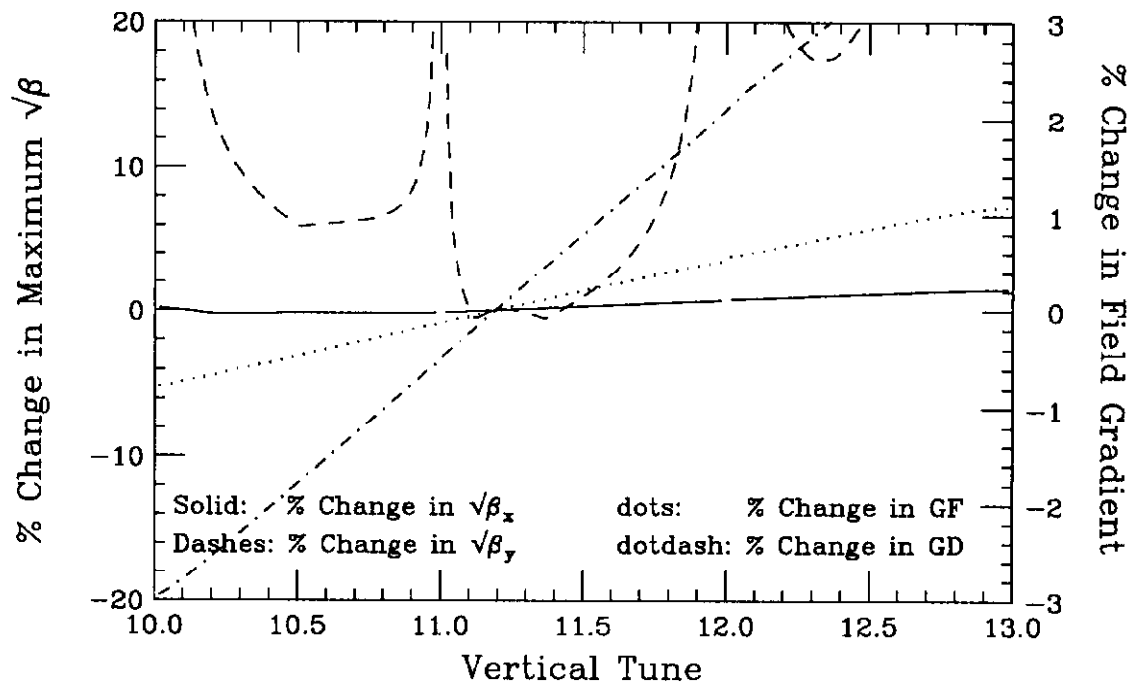


Figure 23

FIG. 23. Betatron-function ($\sqrt{\beta_x}$ and $\sqrt{\beta_y}$) dependences on the vertical tune, the horizontal tune being kept constant.

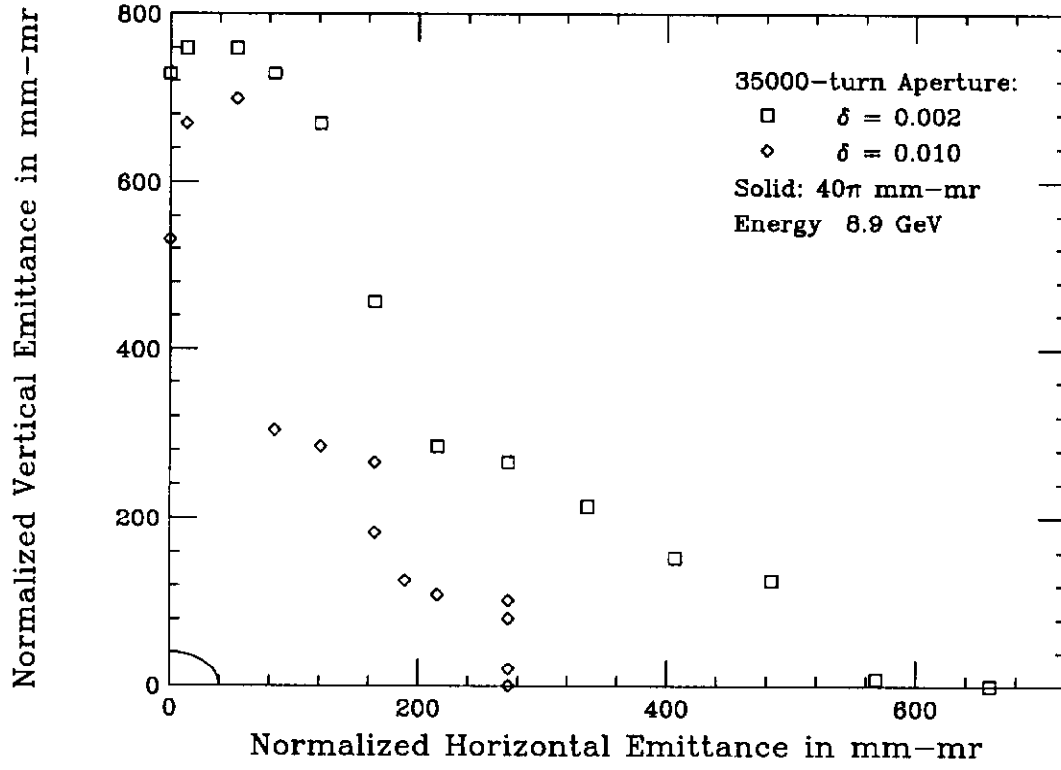


Figure 24

FIG. 24. Dynamical apertures obtained from tracking 35000 turns at the injection energy 8.9 GeV at momentum offsets 0.2% and 1.0%. The required aperture is 40π mm-mr.

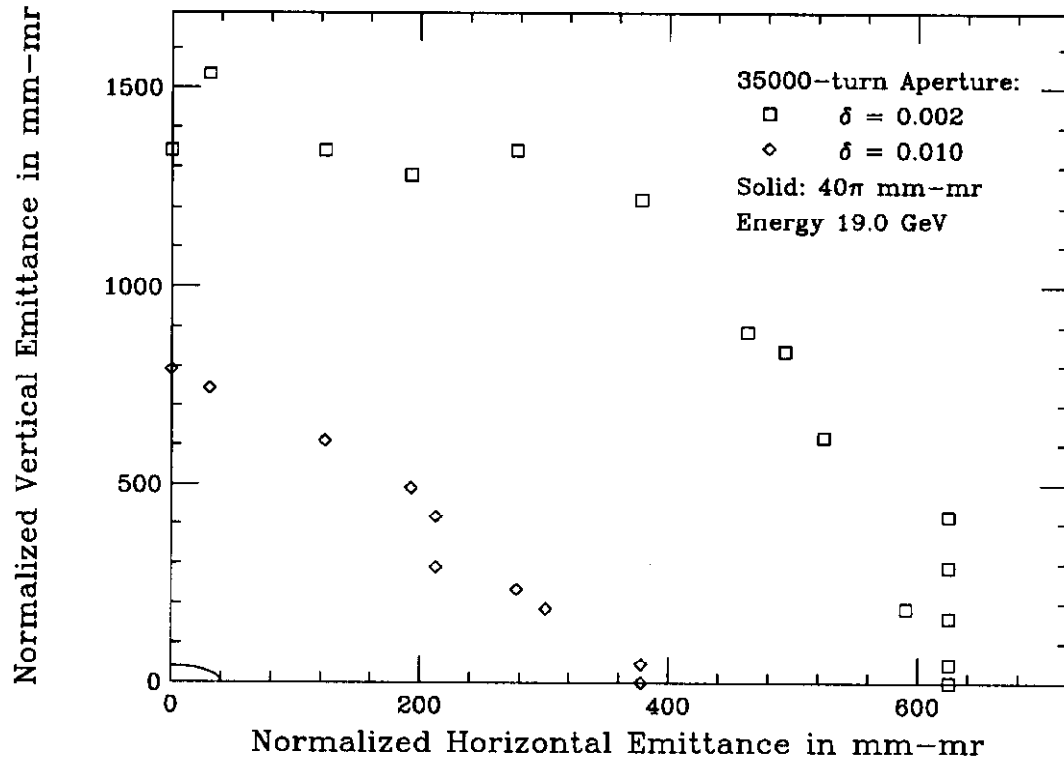


Figure25

FIG. 25. Dynamical apertures obtained from tracking 35000 turns at the 19 GeV at momentum offsets 0.2% and 1.0% when the magnetic field in the dipoles produces the maximum eddy currents.

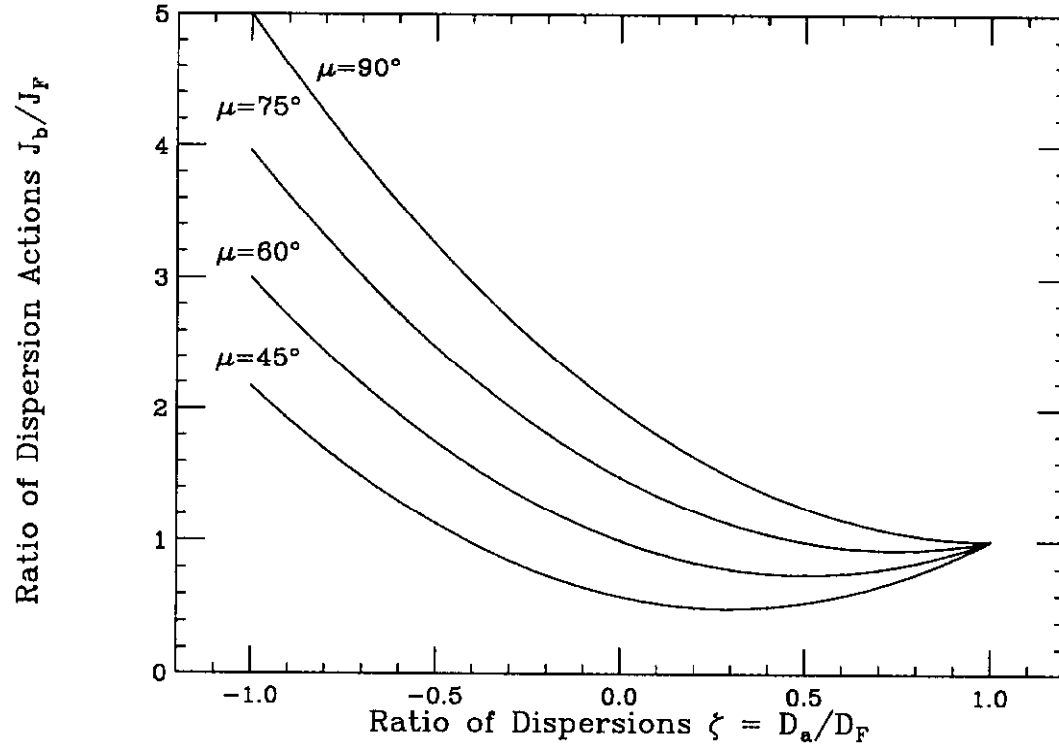


Figure 26

FIG. 26. Ratio of dispersion actions J_b/J_F as a function of $\zeta = D_a/D_F$ for various phase advances μ in the FODO cell.

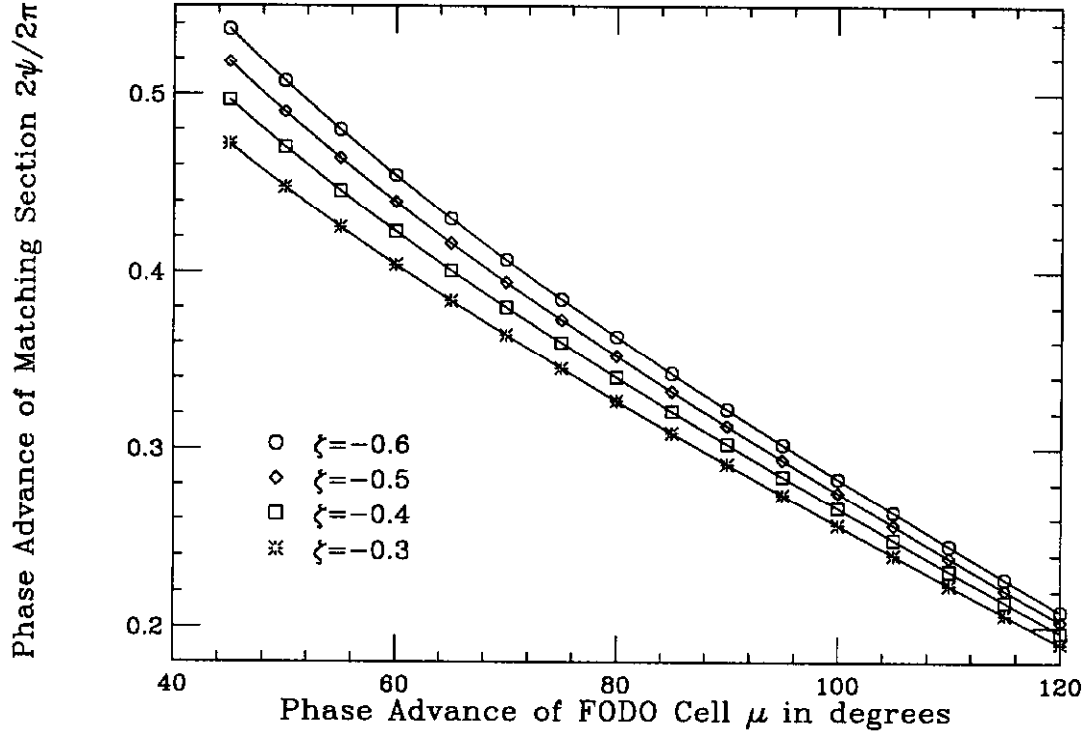


Figure 27

FIG. 27. Phase advance in the matching section as a function of phase advance μ in the FODO cell for various $\zeta = D_a/D_F$.

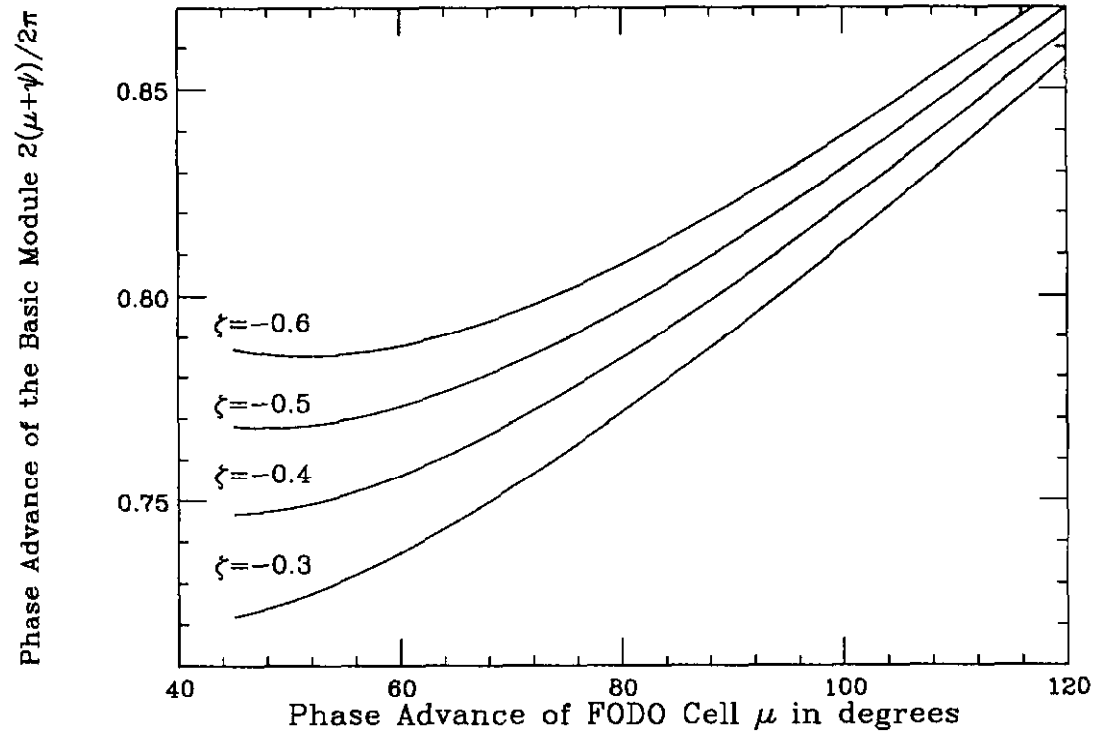


Figure 28

FIG. 28. Total phase advance of the whole module as a function of phase advance μ in the FODO cell for various $\zeta = D_a/D_F$.